TECHNICAL REPORT

For the period: March 15, 1989 - March 1, 1990
Under Contract No. : N00014-89-J-1267 (10/1/88 - 9/30/90)

AD-A222 934

A THEORETICAL STUDY OF FLOW STRUCTURE AND RADIATION FOR MULTIPHASE TURBULENT DIFFUSION FLAMES

S.H. CHAN, C.F. CHERN

Prepared for the Department of the Navy
Office of Naval Research
Arlington, VA 22217

UWM
TM

Department of Mechanical Engineering
University of Wisconsin—Milwaukee
P.O. Box 784
Milwaukee, Wisconsin 53201
March 1, 1990

90 06 11 109

A THEORETICAL STUDY OF FLOW STRUCTURE AND RADIATION FOR MULTIPHASE TURBULENT DIFFUSION FLAMES

S. H. Chan[1] and C. F. Chern[2]
Department of Mechanical Engineering
University of Wisconsin--Milwaukee
P.O. Box 784
Milwaukee, Wisconsin 53201

TECHNICAL REPORT

March 1, 1990

Accesion For	
NTIS CRA&I	☑
DTIC TAB	☐
Unannounced	☐
Justification	
By per call	
Distribution /	
Availability Codes	
Dist	Avail and/or Special
A-1	

STATEMENT "A" per Dr. Gabriel Roy
ONR/Code 1132P
TELECON   6/18/90   VG

1. Wisconsin Distinguished Professor
2. Graduate Student

278E/5574E

TABLE OF CONTENTS

ABSTRACT

The present technical report summarizes the progress made in considering thermal radiation in the analysis of multiphase turbulent flow structure of a halogren gas jet reacts with a liquid metal. The content herein is based on the M.S. dissertation submitted by C.F. Chern, Department of Mechanical Engineering, University of Wisconsin-Milwaukee.

The reaction of a halogen gas jet submerged in an akali liquid metal fuel forms a complex diffusion flame. The flame is turbulent and multiphase in nature and its temperature is relatively high. The purpose of this study is to account for thermal radiation and the radiation/turbulent interaction in analyzing such a diffusion flame structure.

A method is hereby proposed to consider the turbulence-radiation interaction in the analysis of a multiphase diffusion flame. Application is made to study the reaction of a halogen gas jet submerged in an alkali liquid fuel bath. The analysis makes use of a k-ε-g turbulence model, a local homogeneous two-phase model, a chemical equilibrium combustion model, a probabilistic approach and a radiation model compatible with mixture fraction fluctuation. The equilibrium state relationships for instantaneous properties, required for mean scalar property predictions and structure analysis of the reacting jet, have been generated. The energy equation containing the radiative source term has been solved simultaneously with the Favre-averaged transport equations. Numerical results are presented for the specific reactants--chlorine gas as oxidant and liquid sodium as fuel. In comparison to the adiabatic case in which thermal radiation is neglected, the results reveal that thermal radiation greatly affects the plume envelope and the turbulent flame structure.

ACKNOWLEDGMENTS

LIST OF TABLES

LIST OF FIGURES

NOMENCLATURE

C_μ	constant used in turbulent viscosity
$C_{\epsilon 1}$, $C_{\epsilon 2}$	constants used in turbulent dissipation rate
C_{g1}, C_{g2}	constants used in the square of mixture fraction fluctuation
D	droplet diameter
d	diameter of nozzle
e	emissive power
f	mixture fraction
g	the square of mixture fraction fluctuation
H	enthalpy
k	turbulent kinetic energy
K_a	absorption coefficient
K_s	scattering coefficient
L_e	mean beam length
N_i	the number of moles species
P	pressure
$\nabla \cdot q_R$	radiation source term
T	temperature
u	axial velocity
v	radial velocity
x	axial distance

Greek Symbols

μ	molecular viscosity
μ_{eff}	effective viscosity
μ_t	turbulent viscosity
ϕ	conserved scalar quantity

ε	turbulent dissipation rate
σ_k	turbulent Prandtl Number in k equation
σ_ε	turbulent Prandtl Number in ε equation
σ_f	turbulent Schmit Number in f equation
σ_g	turbulent Schmit Number in g equation
ρ	density
ε_i	species emissivity
ε_h	emissivity
ψ	stream function

Superscripts

~	Favre averaged quantities
−	time averaged quantities

Subscripts

i	i species
o	jet nozzle condition
∞	bath (or surrounding) condition
S	solid
L	liquid
G	gas
b	black surface
E	external boundary
I	inner boundary

1. INTRODUCTION

The recent interest in stored chemical energy propulsion systems uses a closed combustor in which thermal energy is generated by the reaction of a halogen gas with an alkali liquid metal. The halogen gas is injected into the combustor filled with the alkali molten metal, forming a complex, turbulent, multiphase diffusion-like flame. Prior study of this type of flame is rather limited (Avery and Faeth 1974, Chen and Faeth 1983, Chan et al. 1988) and none has yet considered thermal radiation effects, in spite of the high temperature mixture in the flame.

Prior studies on turbulence-radiation interaction in combustion are confined to a single-phase, gaseous flame. Notable is Tamanini's work (1977) which assumes that the net rate of volumetric radiative heat loss is a fixed fraction of the local rate of the heat of reaction. The thermal radiation term is in essence eliminated from the energy equation by combining it with the reaction heat source term to circumvent problems arising from turbulence-radiation interactions. Kounalakis et al. (1988), recently examined the effect of concentration fluctuations on the radiation intensity emitted from a gaseous flame by a stochastic technique which simulates scalar property variations along the radiation path. The reverse effect of radiation on turbulence was not investigated. The present study intends to account for the coupled effects of turbulence-radiation interaction in the analysis of multiphase, liquid metal-fuel combustion.

Many existing radiative transfer techniques (Chan 1987) cannot be directly adopted for the analysis of a liquid metal combustion jet due to a number of difficulties. Being a turbulent, multiphase and high temperature flame, the species concentrations in the flame, for example, vary greatly and

fluctuate rapidly so that only mean variables can be derived from the solution of mean conservation equations. Thus a compatibility problem is encountered when any radiative transfer technique is used since radiative transfer is based on instantaneous variables. Furthermore, when radiative transfer is considered, the flame becomes non-adiabatic and enthalpy becomes a nonconserved scalar. The powerful Shvab-Zel'dovich formulation of the conservation equations is unobtainable so that the energy equation needs to be solved explicitly and simultaneously with other conservation equations. Another difficulty is associated with the equilibrium state relationships which will become a function of two variables (say enthalpy and mixture fraction) rather than one variable as in the adiabatic flame case. Thus, new equilibrium state relationships have to be constructed. Finally, the evaluation of mean scalars by a probability density function (PDF) technique becomes troublesome because the PDF is now a function of two variables as well. All these difficulties will have to be resolved in order to include thermal radiation in the analysis of a turbulent diffusion flame in liquid metal combustion.

The primary purpose of the present work is to provide a methodology by which the coupled effect of turbulence-radiation interaction in multiphase reacting flames can be studied. The proposed method overcomes the difficulties mentioned above. To illustrate the essence of the method with quantitative results, a specific pair of reactants is selected--chlorine gas as an oxidant and liquid sodium as a fuel. Since these reactants were investigated previously (Chen and Faeth 1983), their results can be used for comparison in the limiting case of an adiabatic flame when radiative transfer is neglected.

2. METHOD OF ANALYSIS

2.1 Transport Equations

Consider a steady, axisymmetric submerged halogen (or halogenated) gas jet discharging at a choked speed into a large liquid alkali metal pool. The reaction between the halogen gas, the oxidant, and the liquid alkali metal, the fuel, forms a multiphase turbulent diffusion-like flame. Following the previous works (Chen and Faeth 1983, Chan et al. 1988), the local homogeneous flow two-phase model and k-ϵ-g turbulent model are adopted here. The exchange coefficients of species are assumed to be equal and thermodynamic equilibrium be maintained at each point in the flow. The Favre-averaged, (indicated by the superscript ($\sim$)), transport equations to be solved are summarized in Table 1. They include the equations for the mean axial velocity $\tilde{u}$, mixture fraction $\tilde{f}$, turbulence kinetic energy k, turbulence dissipation rate ϵ, the square of mixture fraction fluctuations g, and the stagnation enthalpy $\tilde{H}$. Readers are refered to the previous study (Chan et al. 1988) for explanation of notations. The major difference from the earlier studies lies in the addition of the energy equation, in which the stagnation enthalpy is the dependent variable and a radiation source term has been included. The stagnation enthalpy can be approximated by the static enthalpy because the kinetic energy is small in comparison to the energy release of the reaction.

$\nabla \cdot q_R$ in the energy equation is a Favre-averaged quantity. It involves an integration of directional intensities over 4π solid angles. Each directional intensity can be evaluated stochastically as done by Kounalakis et al. (1988). However, three-dimensionality of the intensity and the presence of multi-species in multiphase make this rigorous approach unpractical because of excessive computational time required at each grid

- 3 -

point. A great simplification can be made if a radial one-dimensionality assumption is invoked (Grosshandler and Bhattacharjee, 1987), which is compatible with the current parabolic, boundary layer type of flow. The assumption is reasonable since flame is often thin and elongated in shape. Further simplification can be made when deemed necessary to reduce the computational time.

In the present turbulence/radiation interaction (called coupled) analysis, the flow properties can be found by solving the transport equations for $\tilde{u}$, $\tilde{f}$, g, k, ε and $\tilde{H}$. Other local mean scalars $\tilde{\phi}$, (such as the mean species mass fraction, mixture temperature and density) can be evaluated by a PDF averaging technique with some stipulation. Since ϕ is now a function of f and H it is assumed (Abou-Ellail et al. 1978) that, in as far as the evaluation of these mean scalars is concerned, the instantaneous variation of H and f at the i-th grid point can be approximated by

$$H = H_\infty + f(\tilde{H}_i - \tilde{H}_\infty)/\tilde{f}_i \quad \text{for } 0 < f < \tilde{f}_i$$

$$= \tilde{H}_i + (f - \tilde{f}_i)(\tilde{H}_0 - \tilde{H}_i)/(1-\tilde{f}_i) \text{ for } \tilde{f}_i \leq f \leq 1$$

(1)

which is shown in Fig. 1. Then the mean scalars, like Favere mean quantities, are evaluated from

$$\tilde{\phi} = \int_0^1 \phi(f,H(f, \tilde{f}_i, \tilde{H}_i)) \, P_F(f, \tilde{f}_i, g)df$$

(2)

where P_F is the clipped Gaussian PDF profile (Lockwood and Naguib 1975) and ϕ is the scalar equilibrium state relations needed to be constructed next.

2.2 Equilibrium State Relationships

Perhaps the foremost complexity introduced by the inclusion of radiative transfer in the analysis is that the mixture enthalpy is no longer a conserved property and that other scalars at any location will be governed by two variables, mixture fraction f and enthalpy H, instead of f alone.

The equilibrium mixture after reaction may be of multiphase, containing ideal or nonideal solutions with electrolytic or non-electrolytic constituents. Its equilibrium temperature, density, void fraction and mass species fraction in all phases should be calculated as a function of the mixture fraction f and the mixture enthalpy H, over an entire range of f ($0 \leq f \leq 1$) and H ($H_o \leq H \leq H_\infty$). The subscripts o and ∞ designate the nozzle exit (f=1) and bath fluid (f = o) conditions. These equilibrium state relationships can be constructed using the CEC-NMS equilibrium code recently developed in this laboratory (Chan et al. 1988).

2.3 Summary of the Methodology

Starting from the nozzle inlet condition, the Favre mean radiative source term a⁺ the first axial, downstream location is calculated by a stochastic technique based on upstream radial conditions. This is calculable in view of the radial one-dimensionality assumption. With the resulting radiative source term, the transport equations listed in Table 1 are solved to yield dependent variables, like $\widetilde{f}_i$ and $\widetilde{H}_i$, etc., at the first downstream location. With equations (1-2) and the equilibrium state relationships $\phi = \phi$ (f,H), other mean scalars not yet solved are calculated. If desired, iteration can be made using new $\bar{p}$ and $\nabla \cdot q$ based on the downstream condition. The procedure is repeated at the next downstream location. Since the radiative source is calculated by a stochastic technique, the effect of turbulence on radiation is accounted for. More importantly, when the radiative source term is

substituted into the energy equation which is then solved simultaneously with the turbulence momentum, K and ϵ equations, they are coupled through $\tilde{u}$, $\tilde{v}$, μ_t and $\bar{\rho}$ present in those equations. The effect of radiation (through $\bar{\rho}$ in $\tilde{u}$, k and ϵ eqs.) on turbulence and the effect of turbulence (through $\tilde{u}$, $\tilde{v}$ and μ_t in $\tilde{f}$ and $\tilde{H}$ eqs.) on radiation are further considered. The latter is apparent since local $\tilde{f}_i$ and $\tilde{H}_i$ are used (see Eq. 1) to evaluate the fluctuating f and H quantities, which in turns are employed to calculate the instantaneous species compositions, temperature and, consequently, the instantaneous radiation properties and intensity. Finally, phase change and chemical reaction are coupled to radiation and turbulence through the use of the equilibrium state relationships. Thus the method proposed indeed accounts for turbulence, radiation, phase change and reaction interactions.

3. CHLORINE JET SUBMERGED IN LIQUID SODIUM

To illustrate the essence of the methodology, consider the steady reaction of an axisymmetric chlorine gas jet discharged at a choked speed from below into a large molten sodium pool. The needed information for computation is presented next.

3.1 Equilibrium State Relationships

For Cl_2/Na reactions, the possible species in the gas phase are $Cl_{(G)}$, $Cl_{2(G)}$, $Na_{(G)}$, $Na_{2(G)}$, $NaCl_{(G)}$ and $Na_2Cl_{2(G)}$. Similarly, the species in the liquid phase are $Na_{(L)}$ and $NaCl_{(L)}$, and the species in the solid phase are $Na_{(S)}$ and $NaCl_{(S)}$. The new equilibrium state relationships of the mixture temperature, density and mass fractions of all species have been constructed as a function of f and H, and are illustrated in Figs 2 to 19. The conditions before the reaction are $T_0 = 298$ K (the oxidant temperature), $T_\infty = 1130$ K (the fuel temperature) and $P_0 = 1$

atm. The distribution of any quantity as a function of f tends to be similar at different stagnation enthalpies. The temperature profiles at different enthalpies reach a maximum when f approaches 0.606, the stoichiometric condition. Density is higher when f approaches 0 where liquid metal is the dominant phase. Most of gases are Cl_2, NaCl and Na. The NaCl gas product reaches the maximum when Cl_2 and Na gases disappear. In the liquid phase, $Na_{(L-1)}$ and $NaCl_{(L-2)}$ are dominant species. The subscripts (L-1) and (L-2) designate, the metal-rich and salt-rich liquids due to the partial miscibility of the metal with the salt. Little Na solid are produced in the chemical equilibrium reaction.

In an adiabatic reaction, the final enthalpy of the product is equal to the initial enthalpy of the reactants and the state relationships are simply given by the two-dimensional profile in the plane normal to and intersecting the H-f plane along the line $H = f H_0 + (1-f) H_\infty$. The results of this special case are shown in Figs. 20-22 which agree with those reported by Chen and Faeth (1983).

3.2 Radiation Properties and Source Term

Most radiation properties of the sodium chloride and other products of Na/Cl_2 reaction are unavailable. Besides, those media are highly nonhomogeneous because of complex flame structures. Therefore, several assumptions are necessarily made. Those assumptions though may appear sometimes inconsistent are introduced in this subsession merely to arrive at an order of magnitude estimation of radiation properties.

The adiabatic flame structure is computed first by neglecting radiative heat transfer and by solving all except the energy equation as done in previous studies (Chen and Faeth 1983, Chan et al. 1988). Among others, the adiabatic calculation yields the flame envelope and mixture fraction profiles

in the flame. Then on the basis of mixture fraction profiles, the flame envelope, as shown in Fig. 23 and Table 2, is subdivided into two segments in the axial direction and five segments in the radial direction for a total of ten sublayers. The mean radiation properties in each sublayer are estimated next.

In the Na/Cl_2 reaction, the primary radiation participating species are $Na_{(L)}$, $NaCl_{(L)}$, $NaCl_{(S)}$, $NaCl_{(G)}$ and $Na_2Cl_{2(G)}$. $NaCl_{(S)}$ mass fraction is relatively small and can be neglected.

To calculate the absorption and scattering coefficients attributable to the liquid phase, the mass of each liquid species ($Na_{(L)}$ and $NaCl_{(L)}$) in each sublayer is calculated as presented in Table 3. The liquid species are assumed to exist in droplet form. Since the droplet diameter and density can't be predicted accurately, the diameter is estimated by a Weber number droplet break-up criterion $D_i = 12\sigma/\rho_0 u_0^2$. With the droplet size and liquid mass determined, the droplet density of species i, N_i, in each sublayer can be calculated (see Table 4). The absorption and scattering coefficients are then evaluated using the large particle limit model (i.e. $\pi D_i/\lambda \geq 5$, λ being radiation wave-length),

$$K_{a_i} = N_i \, \epsilon_{hi} \, \pi \, D_i^2/4, \quad K_{s_i} = N_i \, \rho_{hi} \, \pi \, D_i^2/4 \tag{3}$$

For a liquid sodium at 1130 K, $\epsilon_{h,Na(L)}$ and $\rho_{h,Na(L)}$ are found from Chan and Tseng (1979). As to a NaCl liquid droplets, its value is approximated by that of a large ideal dielectric sphere. The absorption and scattering coefficients of the liquid droplets are summarized in Table 5.

The absorption coefficient of a gas species is calculated from the sublayer mean beam length L_e and the species emissivity $\epsilon_{i(G)}$ by

$$K_{a,i(G)} = - \ln (1 - \epsilon_{i(G)})/L_e \qquad (4)$$

In the absence of data on emissivities of $NaCl_{(G)}$ and $Na_2Cl_{2(G)}$ their orders of magnitude are arbitrarily approximated by that of a triatomic gas, say, water vapor, at the same temperature and pressure path length $(P_{ei}L_e)$ conditions. The estimated absorption coefficient of the gas phase is given in Table 6.

Finally, by summing up the contributions from all species in all phases, the mixture absorption and scattering coefficients in each of the ten sublayers are yielded and summarized in Table 7. The scattering coefficient is included here for later study.

Similarly, a simplified radiative source expression is desirable. Under the planar approximation, the source term $\Delta.q_{rad}$ in an absorbing, emitting and scattering medium is [Sparrow and Cess, 1978]:

$$\Delta.q_{rad} = [\frac{4K_a}{K_a + K_s} e_b(X) - \frac{K_a}{K_a + K_s} G(X) - 2q_{0,1} - 2q_{0,2}] (K_a + K_s) \qquad (5)$$

$$q_{0,1} = \frac{\epsilon_1 e_{b1} + (1 - \epsilon_1)\epsilon_2 e_{b2}}{1 - (1 - \epsilon_1)(1 - \epsilon_2)} \qquad (6)$$

$$q_{0,2} = \frac{\epsilon_2 e_{b2} + (1 - \epsilon_2)\epsilon_1 e_{b1}}{1 - (1 - \epsilon_1)(1 - \epsilon_2)} \qquad (7)$$

$$G(X) = 2\pi \int_0^1 i^+(0,\mu)e^{-x/\mu}d\mu + 2\pi \int_0^1 i^- e^{(x_0-x)/\mu}d\mu$$

$$+2 \int_0^{x_0} [\frac{K_a}{K_a + K_s} e_b(t) + \frac{K_s}{4(K_a + K_s)} G(t) E_1(|X-t|)dt \qquad (8)$$

For the optically thin limit, the final form of Eq. (5) becomes

$$\nabla \cdot q_{rad} = 2K_a [2e_b - (q_{o,1} + q_{o,2})] \tag{9}$$

If the wall emissivities ($\epsilon 1$ and $\epsilon 2$) and temperature (T_{b1} and T_{b2}) are the same, then $q_{o,1} = q_{o,2} = e_{b1} = e_{b2} = e_{b,surr}$ and

$$\nabla \cdot q_{rad} = 4K_a \sigma (T^4 - T_\infty^4) \tag{10}$$

in which surface properties and the scattering coefficient vanish nicely. In Eq. (10), T_{surr} is the bath temperature and K_a, the absorption coefficient, has been calculated and listed in Table 7. Equation (10), though derived from the planar layer, is equally applicable for the cylindrical geometry. This approximation is adopted here since the current axisymmetric flame is elongated and optically thin radially. Gross estimation of K_a values seems to render unnecessary the evaluation of the Favre averaging of ($\nabla \cdot q_R$) by a rigorous stochastic technique. Rather the local K_a and T are approximated by the mean values of the local sublayer to reduce the excessive computation time in this preliminary investigation.

3.3 <u>Boundary and Initial Conditions</u>

The uniform Cl_2 inlet conditions at the nozzle (diameter, d = 7.9 x 10^{-4}m) exit are ρ_0 = 2.898 kg/m^3, T_0 = 298 K, $\widetilde{u}_0$ = 203.4m/s, k_0 = $(0.03\widetilde{u}_0)^2$, ϵ_0 = $(0.03\widetilde{u}_0)^3/d$, $\widetilde{f}_0$ = 1, g_0 = 0, $\widetilde{H}_0(T_0)$ = 64.22 J/kg. The sodium bath conditions are T_∞ = 1130 K and P_∞ = 10^5 Pa. In the outer free boundary (the Nth grid point) of the reacting plume, $\widetilde{u}_N$ = 0.0005 $\widetilde{u}_0$, $\widetilde{f}_N$ =0.0005, g_N = 0, $\widetilde{H}_N(T_\infty)$ = 1.188 x 10^6 J/kg while k_N and ϵ_N, are obtained by solving the governing equations while neglecting the radial convective and diffusive terms as follows:

$$k_{d,N} = k_{u,N} - \epsilon_{u,N} \, \Delta x / \tilde{u}_{u,N} \tag{11}$$

$$\epsilon_{d,N} = \epsilon_{u,N} - C_{\epsilon 2} \epsilon_{u,N}^2 \, \Delta x / (k_{u,N} \, \tilde{u}_{u,N}) \tag{12}$$

In the above, $\tilde{H}_0$ and $\tilde{H}_N$ are enthalpies of pure chlorine and pure liquid sodium, subscripts (d,N) and (u,N) denote downstream and upstream of Nth grid point, and Δx is the step size in the jet axial direction.

The gradient of the dependent variable is set to zero for the inner symmetrical boundary along the center jet axis, $\partial \tilde{\phi} / \partial r = 0$, where $\tilde{\phi} = \tilde{u}$, $\tilde{f}$, g, k, ϵ and $\tilde{H}$ from the adiabatic flame structure solution.

4. METHOD OF SOLUTION AND RESULTS

4.1 Adiabatic Flame

The flame structure computations were performed using a version of GENMIX code (Spalding, 1977) modified by our team. Before computing the coupled radiation/turbulence interaction, the adiabatic flame structure was computed first, partly for radiation property evaluation and partly for comparison with the existing solution (Chen and Faeth 1983). The variations of the mean properties of temperature, nondimensional velocity, mixture fraction, void fraction and the overall mass fraction of each phase along the dimnesionless axis location, x/d, are shown in Fig. 24. The highest temperature along the axis is about 2950K at x/d=26. This is lower than the highest possible instantaneous temperature because of the use of a clipped Gaussian probability density function. According to the axial void fraction profile in Fig. 24, the flame length (the total penetration length) extends to x/d=150. By referring to Figs. 24 and 25, it is seen that reaction is completed at the position where the temperature reaches its maximum which is nearly at the

stoichiometric condition. The axial variations of the mean species mass fraction in different phases are also plotted in Figs. 25 to 27. In the gas phase, most of species are Cl_2, Na and NaCl. NaCl has the largest amount at x/d=26 where temperature reaches the maximum. This is understandable since the reaction is almost a simple and fast type of reaction at the stoichiometric condition. Most of the liquid phase appear when x/d is greater than 25 in which temperature is lower than the boiling temperatures. As mentioned before, the solid phase occurs only when the mixture fraction approaches 1 where the mixture temperature is much less than the melting temperature of NaCl (1073K). This is shown in Fig. 27. Physically, solid phase exists only near the nozzle location where mixture fraction approaches 1 and temperature is low. The potential core where velocity is approximately equal to or greater than 99 percent of initial velocity terminates at x/d=12. All the calculations are in good agreement with that of Chen and Faeth [1983].

The radial variations of the mean properties of temperature, nondimensional velocity and mixture fraction are also presented in Figs. 28-31. The profiles of the mean mixture fraction and velocity are nearly identical because buoyance effect is neglected in the source term of momentum equation. The form of the momentum equation without a source term is similar to that of mixture fraction equation. The slight difference between mean mixture fraction and velocity is due to different effective viscosity μ_{eff} and boundary conditions used in both equations.

Additional calculations for a pure chlorine injected into a pure liquid sodium at atmospheric pressure indicate that the flow structure and scalar properties are significantly controlled by the ambient temperature because of subcooling effect. Decreasing liquid temperature will increase condensation which in turn reduces the flame length as defined by the void fraction

profile. The effect of subcooling is shown in Figs. 32-33 and Table 8. In Fig. 22, T_∞ is chosen as 902K while in Fig. 33, T_∞ is chosen as 674K. T_0, P_∞ and other conditions are the same as the case of $T_\infty=1130K$.

From the above Figures and Table, we can see the significant effect of subcooling on turbulent diffusion flames of a gaseous oxidizer injected into a liquid metal fuel. The total penetration length will extend to infinity as the liquid sodium approaches its boiling temperature because of the diminishing driving potential for condensation (i.e., no subcooling effect).

4.2 Nonadiabatic Flame with Radiation

The computational results of the coupled turbulence/radiation interaction analysis are given in Fig. 34-37 which show that the flow structure deviates from that of adiabatic case presented above. In Fig. 34, the total penetration length of the plume (defined by the length when the mixture fraction reduces to 0.005 which approximately corresponds to zero void fraction) extends to x/d=123, which is about 18 percent shorter than the adiabatic one. The highest temperature along the center axis is about 2810 K at x/d=23. This is lower than the adiabatic case of 2950 K. The profiles of mixture fraction f and velocity u/u_0 remain similar even when radiation is accounted for in turbulent reacting flow. There exists only the gaseous phase between x/d=16 and x/d=25 where the mixture temperature exceeds the boiling temperature of Na and NaCl. In Figs. 34-37, all quantities shift to the left due to the effect of radiation/turbulence interaction. The differences in the radial temperature and velocity profiles at different x/d between coupled and adiabatic analyses are presented in Figs. 38-39. Figure 38 shows that the velocity difference is small at small x/d locations. This is because the radiation effect is insignificant near the injector where the jet stream

temperature is still low. The difference becomes progressively larger away from the injector. Close to the injector, due to the radiative heating by the surrounding warmer liquid sodium, the jet stream along the jet axis is heated up above the adiabatic case as shown in Fig. 39(a) and (b). But then as the jet temperature increases, the radiative transfer from the jet to the surrounding becomes important and the mixture jet temperature eventually drops below the adiabatic one as illustrated in Figs. 39(c) and (d). By referring to Figs. 24, 34 and 39(c), the maximum temperature difference between the coupled case and the adiabatic case is about 300 K at $x/d=25$. In Figs. 39(c) and (d), due to radiation, the temperature of the coupled case is lower than the adiabatic case near the center axis. Also shown in Figs. 39(c) and (d), the location of second grid point y_2 of te coupled case is slightly farther away from the center axis than that of the adiabatic case. This is because in th GENMIX formulattion [Spalding, 1977, pp 112-113], the y_2 location can be readily shown as

$$y_2 = (\frac{2W_2(\psi_E - \psi_I)}{(\rho u)_2 \psi_I})^{1/2} \tag{11}$$

where $\psi_I = 1$ in the present axisymmetric flow, W_2 is a pre-determined dimensionless stream function at location 2 and $(\psi_E - \psi_I)$ is the entrainment rate. For the coupled case, since the entrainment rate is larger and the velocity u_2 is smaller than the adiabatic case, y_2 is larger accordingly. In addition, all quantities at y_2 in the GENMIX formulation are inherently identical to those at y_1 (=0). This explains the flatness of the curves shown in Figs. 38 and 39.

The differences of the jet profile and plume profile are shown in Figs. 40 and 41, respectively. The jet profile is defined as the envelope

connecting all the Nth grid points (the furthest grid point from the jet axis) while the plume profile is defined similar to the total plume length as the locations where f is reduced to 0.005. At such low values of f, the void fraction is practically zero. Figure 40 shows that the jet profile is not greatly affected by the radiation/turbulence interaction. In Figure 41, the plume profile of the coupled case begins to shrink around x/d=80, much shorter than the adiabatic case which occurs around x/d≈130. Due to the collapsing plume and therefore, the void fraction, the overall jet profiles also begin to shrink to some extent at those x/d values as shown in Fig. 40. This phenomenon is attributed to radiative heat loss which causes a lower mixture temperature. Decreasing mixture temperature will reduce mixture volume under constant pressure condition and therefore shrink the jet envelope.

5. CONCLUSION

A method has been proposed to consider thermal radiation in the analysis of a turbulent multiphase diffusion flame. A specific example is presented for a reacting chlorine gas jet submerged in a molten sodium pool. In the absence of data, thermal radiation properties of Na/Cl_2 reaction products were estimated. New equilibrium state relationships for scalar properties were presented as a function of enthalpy and mixture fraction. Results of flame structure including flame envelope have also been presented. Significant differences in flame structures were found between the adiabatic flame and the non-adiabatic flame which accounts for radiative heat losses. The results of the computation shows a strong turbulence/radiation interaction even under the optically thin condition.

REFERENCES

Abou-Ellail, M. M. M., Gosman, A. D., Lockwood, F. C. and Megahed, I. E. A. 1978, Description and Validation of a Three-Dimensional Procedure for Combustion Chamber Flows, Progress in Astronautics and Aeronautics, Vol. 58, pp. 163-190.

Avery, J. F. and Faeth, G. M. 1974, Combustion of a Submerged Gaseous Oxidizer Jet in a Liquid Metal, 15th Symp. (Int.) on Combustion, pp. 501-512.

Chan, S. H. 1987, Numerical Methods for Multi- dimensional Radiative Transfer Analysis in Participating Media, Annual Rev. Numerical Fluid Mech. and Heat Transfer, ed. T.C. Chawla, Vol. 1, pp. 305-345, Hemisphere, Washington.

Chan, S. H., Janke, P. J. and Shen, T. R. 1988, Equilibrium Computations of Multiphase Nonideal Electrolytic Systems and Structure of Turbulent Reacting Dissolving Jets, 22nd Symp. (Int.) on Combustion, pp. 721-729.

Chan, S. H. and Tseng, H. H. 1979, Thermal Radia- tion Properties of Inter- faces between Nuclear Reactor Material, Nuclear Science and Engineering, 71, pp. 215-227.

Chen, L. D. and Faeth, G. M. 1983, Structure of Turbulent Reacting Gas Jets Submerged in Liquid Metals, Comb. Sci. and Tech., Vol. 11, pp. 101- 120.

Grosshandler, W. L. and Bhattacharjee, S. 1987, A Simplified Model for Compu- tation of the Radiative Source Term in Parabolic Flows, the 24-th National Heat Transfer Conf., HTD-Vol-72, pp. 105-110.

Kounalakis, M. E., Gore, J. P. and Faeth, G. M. 1988, Turbulence/Radiation Interactions in Non- premixed Hydrogen/Air Flames, 22nd Sym. (Int.) on Combustion, pp. 1281-1290.

Lockwood, F. C. and Naguib, A. S. 1975, The Pre- dictions of the Fluctuations in the Properties of Free, Round Jet, Turbulent, Diffusion Flames, Combustion and Flame, Vol. 24, pp. 109-124.

Spalding, D. B. 1977, A General Computer Program for Two-Dimensional Parabolical Phenomena, Pergamon Press, Oxford.

Sparrow, E. M. and Cess, R. D., 1978, Radiation Heat Transfer, p. 219, Hemisphere, Washington.

Tamanini, F. 1977, Reaction Rates, Air Entrainment and Radiation in Turbulent Fire Plumes, Comb. Flame, Vol. 30, pp. 85-101.

TABLE 1. Governing Equations

$$\frac{\partial \overline{\rho}\tilde{u}}{\partial x} + \frac{1}{r}\frac{\partial}{\partial r}(r\overline{\rho}\tilde{v}) = 0$$

$$\overline{\rho}\tilde{u}\frac{\partial \phi}{\partial x} + \overline{\rho}\tilde{v}\frac{\partial \phi}{\partial r} = \frac{1}{r}\frac{\partial}{\partial r}(r\mu_{eff,\phi}\frac{\partial \phi}{\partial r}) + S_\phi$$

ϕ	$\mu_{eff,\phi}$	S_ϕ
$\tilde{u}$	$\mu + \mu_t$	$a(\rho_\infty - \overline{\rho})$
$\tilde{f}$	$(\mu/Sc) + (\mu_t/\sigma_t)$	0
k	$\mu + (\mu_t/\sigma_k)$	$\mu_t(\frac{\partial \tilde{u}}{\partial r})^2 - \overline{\rho}\epsilon$
ϵ	$\mu + (\mu_t/\sigma_\epsilon)$	$[C_{\epsilon 1}\mu_t(\frac{\partial \tilde{u}}{\partial r})^2 - C_{\epsilon 2}\overline{\rho}\epsilon]\frac{\epsilon}{k}$
g	$(\mu/Sc) + (\mu_t/\sigma_g)$	$C_{g1}\mu_t(\frac{\partial \tilde{f}}{\partial r})^2 - C_{g2}\overline{\rho}\frac{\epsilon g}{k}$
$\tilde{H}$	$\mu/S_c + \mu_t/\sigma_H$	$-\nabla \cdot q_{rad}$

C_μ	$C_{\epsilon 1}$	$C_{\epsilon 2}$	C_{g1}	C_{g2}	σ_k	σ_ϵ	σ_f	σ_g	σ_H	S_c
0.09	1.44	1.84	2.8	1.84	1.0	1.3	0.7	0.7	0.7	0.7

$$\mu_t = \overline{\rho}C_\mu k^2/\epsilon$$

locations of regions in radial and axial directions

sublayer No	averaged temperature in each sublayer, K	$\tilde{f}$		radial location y/d							
				axial region							
				0	1	2	3	4	5	6	7
				X/D 0	10	20	30	40	50	60	70
1,6	1300	0.1	(17)	1.36	1.80	2.24	2.67	3.11	3.54	3.98	4.41
		0.2	(16)	1.31	1.68	2.05	2.42	2.79	3.16	3.53	3.89
		0.3	(15)	1.25	1.55	1.86	2.16	2.45	2.77	3.08	3.38
2,7	1750	0.35	(14)	1.21	1.48	1.76	2.03	2.30	2.57	2.85	3.12
		0.4	(13)	1.17	1.42	1.65	1.89	2.13	2.38	2.62	2.86
		0.45	(12)	1.13	1.34	1.55	1.76	1.97	2.18	2.39	2.60
3,8	3250	0.5	(11)	1.08	1.26	1.44	1.62	1.79	1.93	2.15	2.44
		0.55	(10)	1.03	1.18	1.33	1.47	1.62	1.77	1.92	2.06
		0.6	(9)	0.98	1.10	1.21	1.33	1.45	1.57	1.68	1.80
		0.65	(8)	0.93	1.01	1.10	1.19	1.27	1.36	1.44	1.53
4,9	1800	0.7	(7)	0.87	0.93	0.98	1.04	1.09	1.15	1.21	1.26
		0.75	(6)	0.82	0.84	0.87	0.89	0.92	0.94	0.97	0.99
		0.8	(5)	0.76	0.76	0.76	0.76	0.76	0.76	0.76	0.76
		0.85	(4)	0.70	0.66	0.63	0.59	0.55	0.52	0.48	0.45
5,10	300	0.9	(3)	0.64	0.57	0.50	0.44	0.37	0.30	0.29	0.17
		0.95	(2)	0.57	0.48	0.38	0.28	0.19	0.09	0.00	0.00
		0.99	(1)	0.51	0.38	0.25	0.13	0.00	0.00	0.00	0.00

* The number in the parenthesis corresponds to each mixture fraction profile and is numbered outward radially

Table 2: The location and averaged temperature in the combusting flow

sublayer No	1	2	3	4	5	6	7	8	9	10
Na_L	179	0	0	0	0	684	0	0	0	0
$NaCl_L$	151	7.26	0	0	0	558	24.2	0	0	0
$NaCl_G + Na_2Cl_{2G}$	11.9	74.2	96.2	60.5	2.86	41.6	238	264	110	0

unit : $10^{-7}g$

Table 3: The mass of each sublayer

sublayer No	1	2	3	4	5	6	7	8	9	10
Na_L	19124	0	0	0	0	73077	0	0	0	0
$NaCl_L$	4247	268	0	0	0	20590	593	0	0	0

Table 4: The number of particle in each sublayer

sublayer No	1	2	3	4	5	6	7	8	9	10
$K_{a,Na,L}$	0.00036	0	0	0	0	0.00133	0	0	0	0
$K_{s,Na,L}$	0.027	0	0	0	0	0.101	0	0	0	0
$K_{a,NaCl,L}$	0.006	0.0003836	0	0	0	0.029	0.000849	0	0	0
$K_{s,NaCl,L}$	0	0	0	0	0	0	0	0	0	0

unit of K_a and K_s:cm^{-1}

Table 5: The absorption and scattering coefficients of liquid

sublayer No	1	2	3	4	5	6	7	8	9	10
$K_{a,NaCl+Na_2Cl_2,G}$	20.5	24	14	12.6	59.8	8.9	11.5	6.8	6.6	108.4

unit : $10^{-3} cm^{-1}$

Table 6 : The absorption coefficient of gas

Sublayer	1	2	3	4	5	6	7	8	9	10
X/D	0-35	0-35	0-35	0-35	0-35	35-70	35-70	35-70	35-70	35-70
$\tilde{f}$	0-.3	.3-.45	.45-.7	.7-.95	.95-1	0-.3	.3-.45	.45-.7	.7-.95	.95-1.
K_a	26.8	24	14	12.6	59.8	39.3	11.5	6.8	6.6	108.4
k_s	27	0	0	0	0	101	0	0	0	0

Table 7: The mixture absortion and scattering coefficients in combustion field

T_∞, K	1130	902	674
$Flame Length, x/d$	150	25	10.2

Table 8: Comparison of subcooling effect
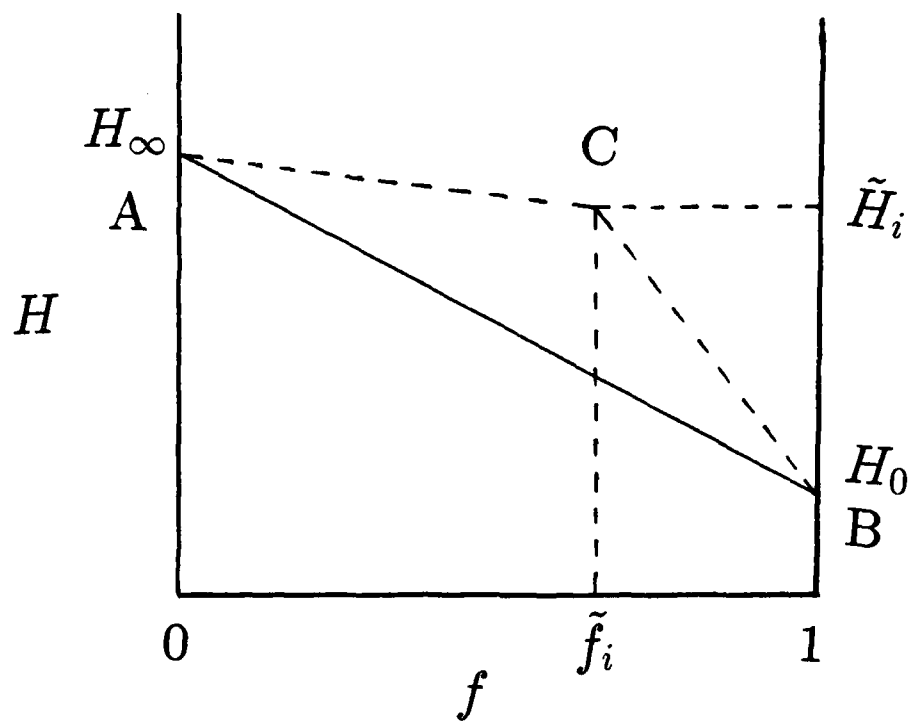
Fig.1 The linearized stagnation enthalpy and mixture fraction
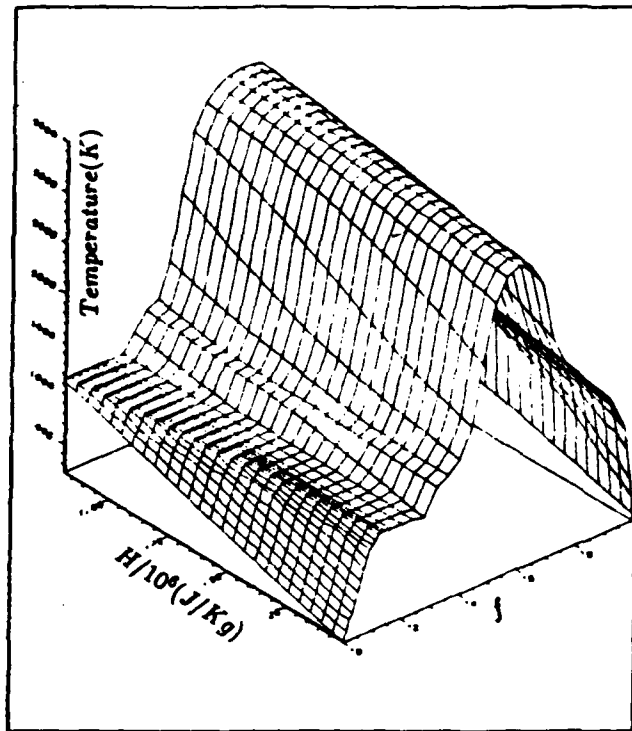
Figure 2 : Temperature distribution with different f and H
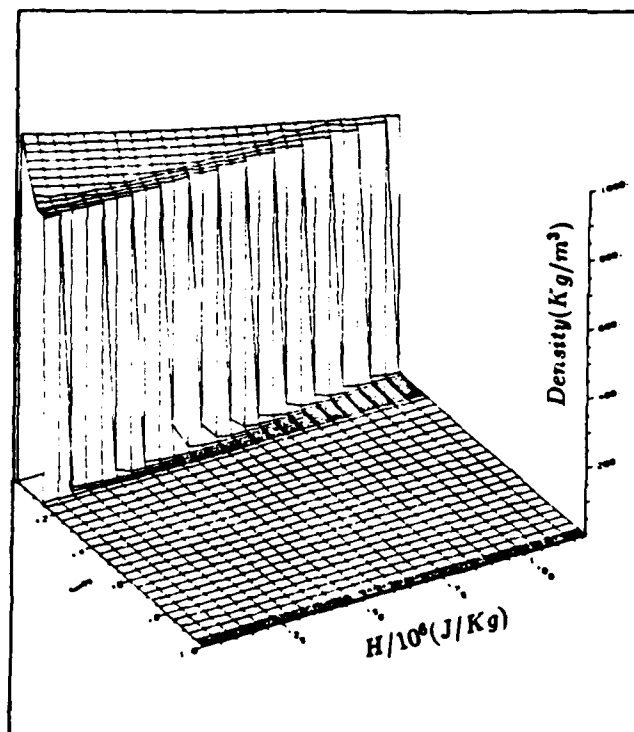
Figure 3 : Density distribution with different f and H
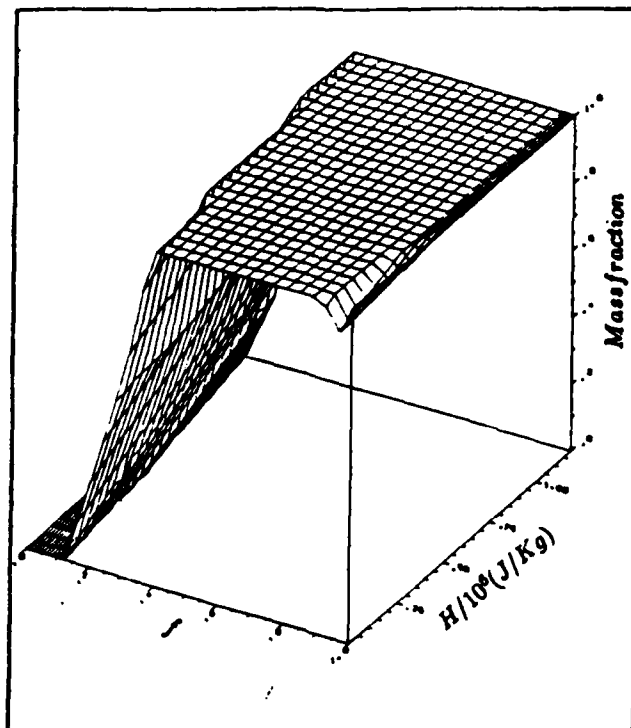
Figure 4 : Y(G) distribution with different f and H
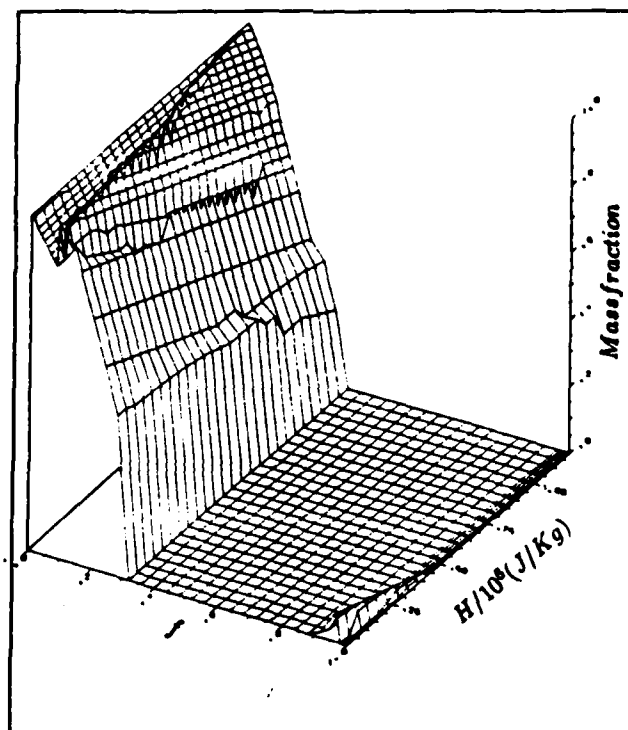
Figure 5 : Y(L) distribution with different f and H
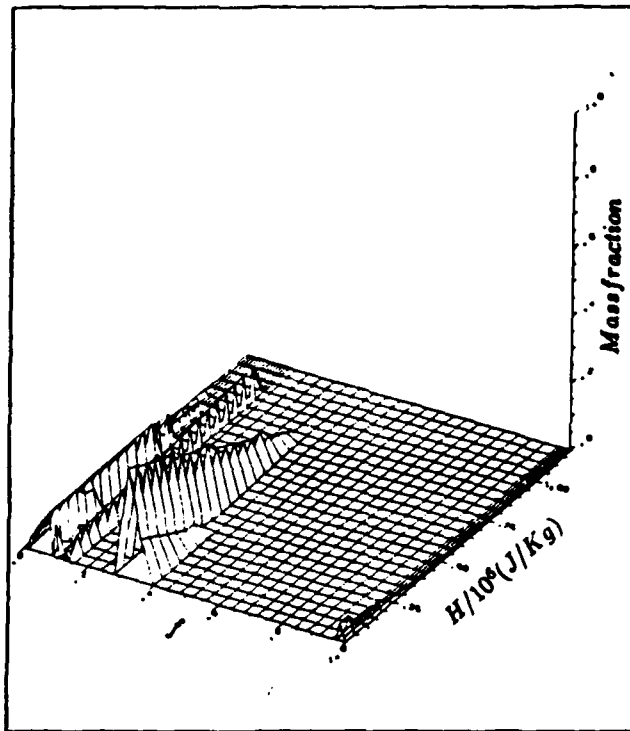
Figure 6 : Y(S) distribution with different f and H
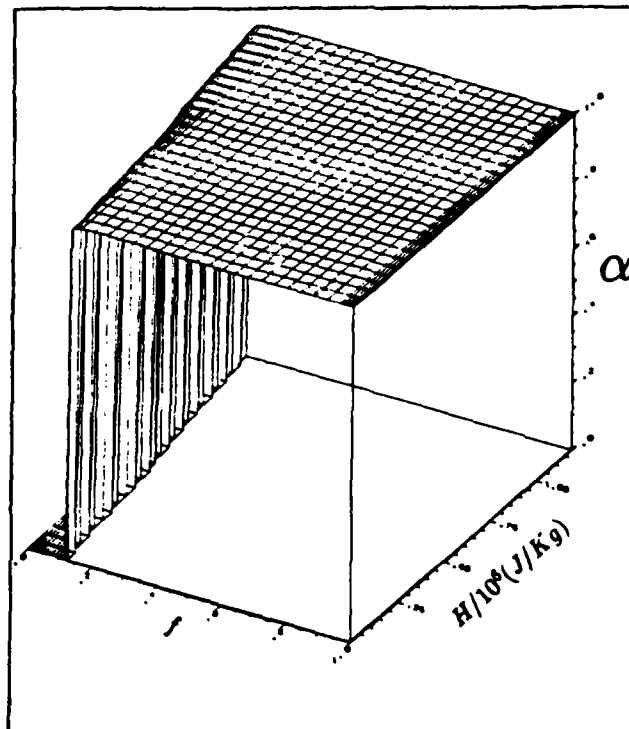
Figure 7: Void fraction distribution with different f and H
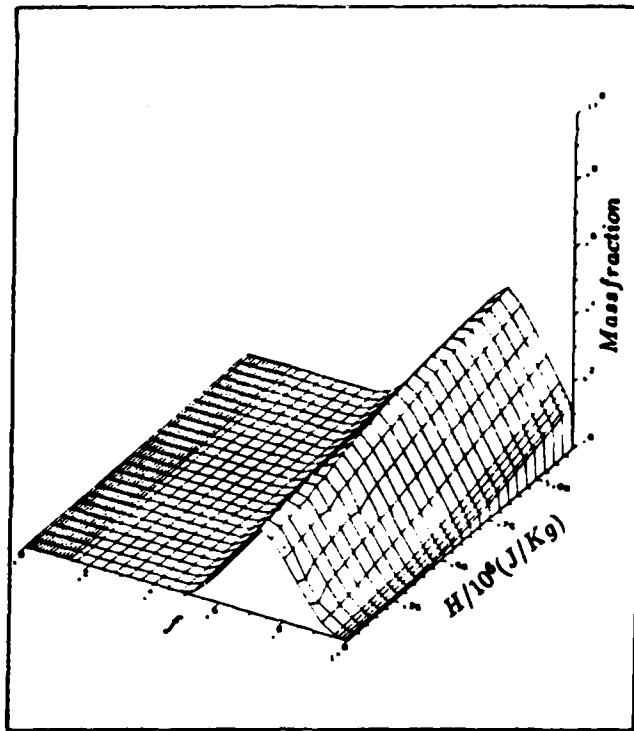
Figure 8: Y(CL,G) distribution with different f and H
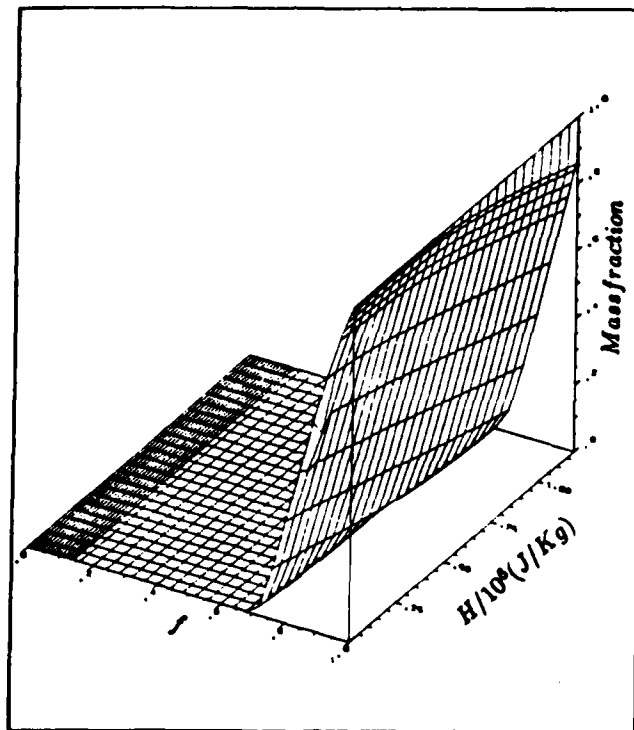
Figure 9: Y(CL2,G) distribution with different f and H
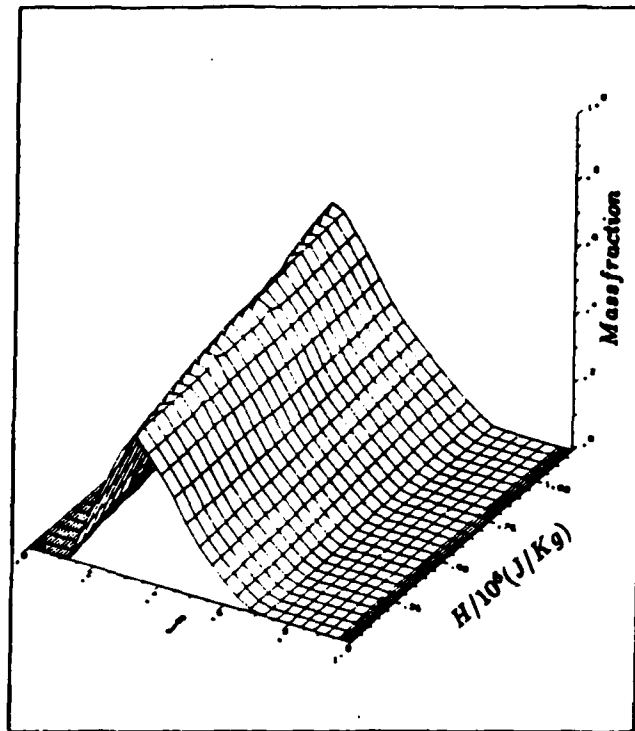
Figure 10: Y(NA,G) distribution with different f and H
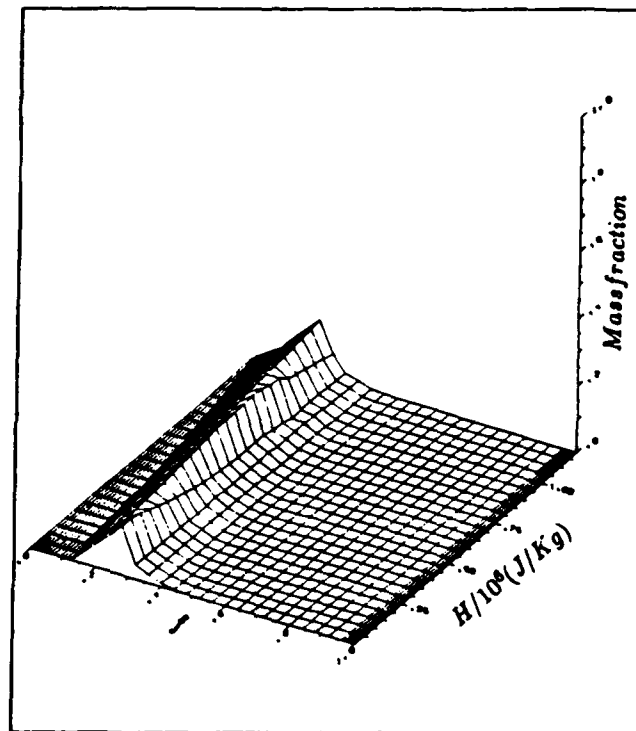
Figure 11: Y(NA2,G) distribution with different distribution f and H
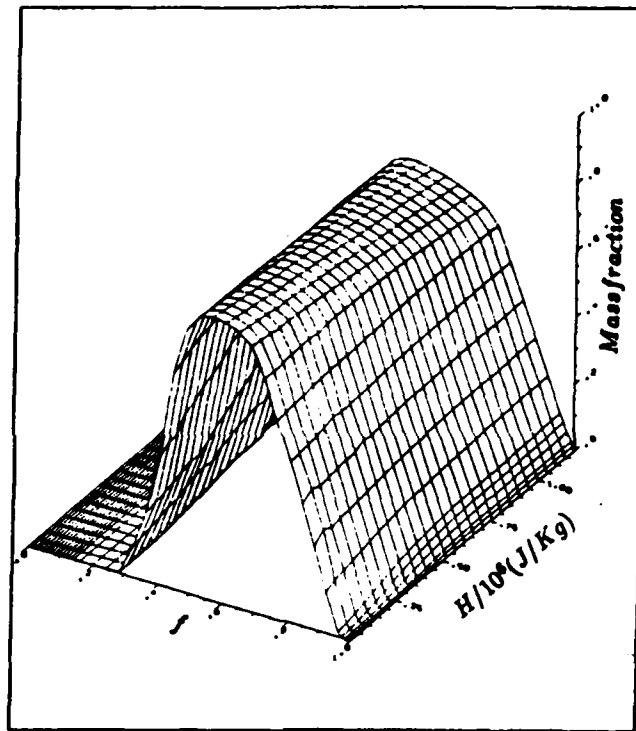
Figure 12: Y(NACL,G) distribution with different f and H
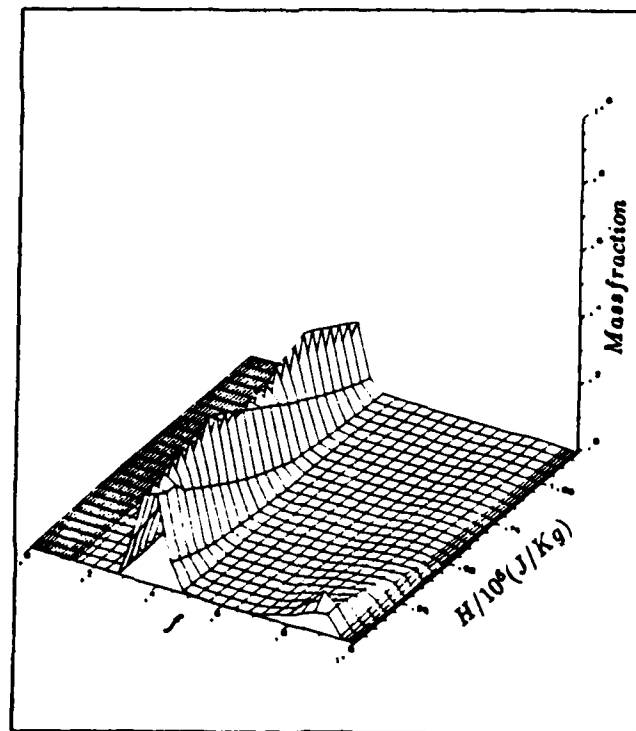
Figure 13: Y(NA2CL2,G) distribution with different f and H
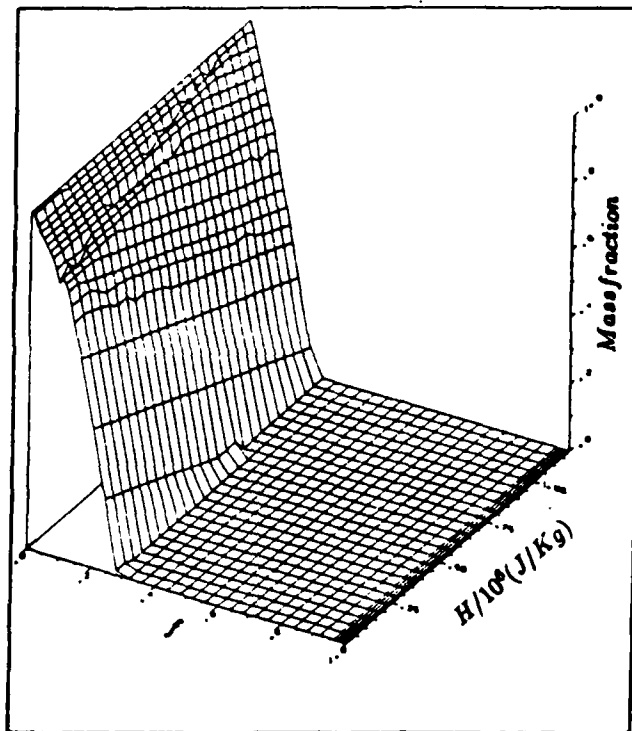
Figure 14: Y(NA,L-1) distribution with different f and H
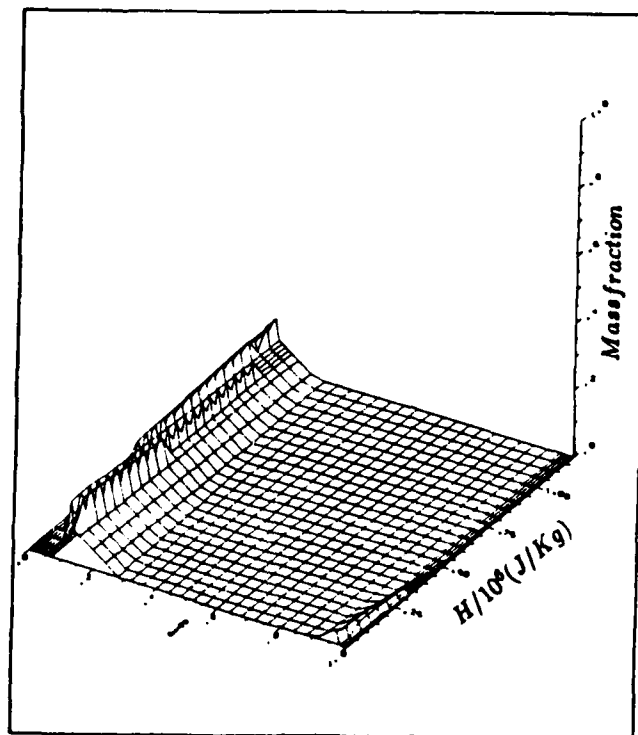
Figure 15: Y(NACL,L-1) distribution with different f and H
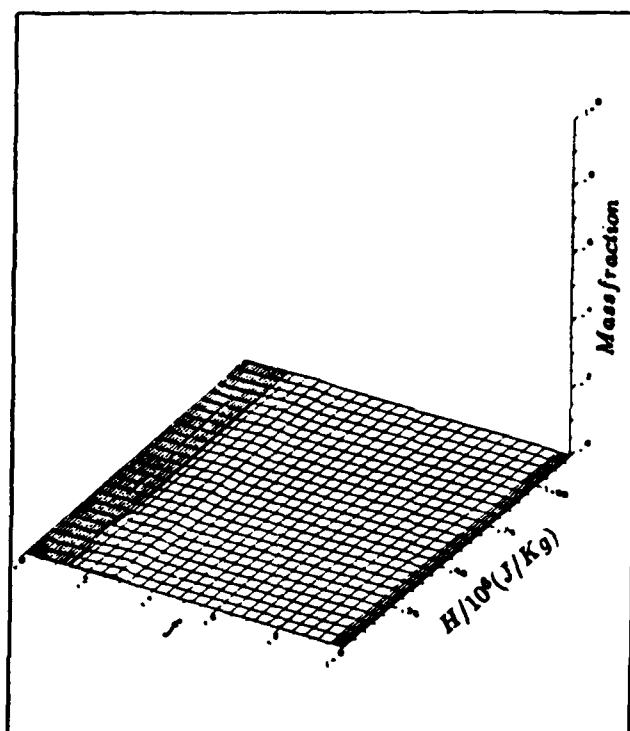
Figure 16: Y(NA,L-2) distribution with different f and H
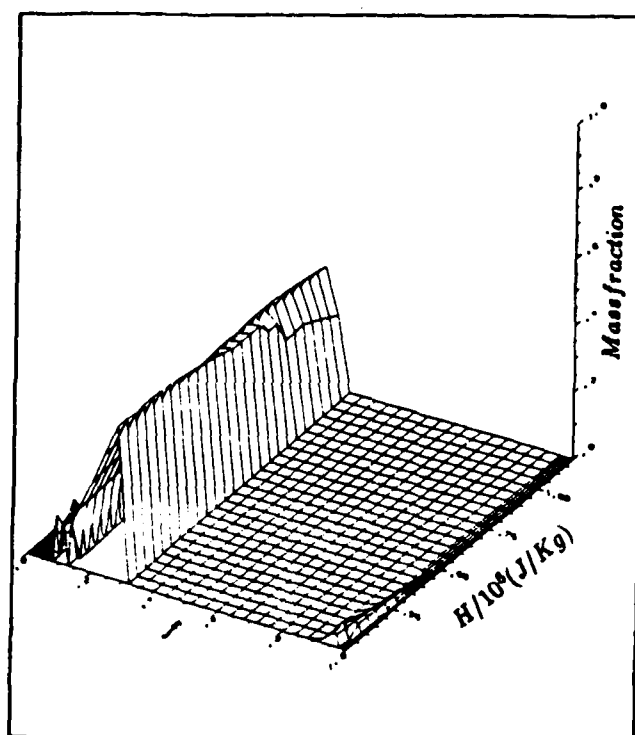
Figure 17: Y(NACL,L-2) distribution with different f and H
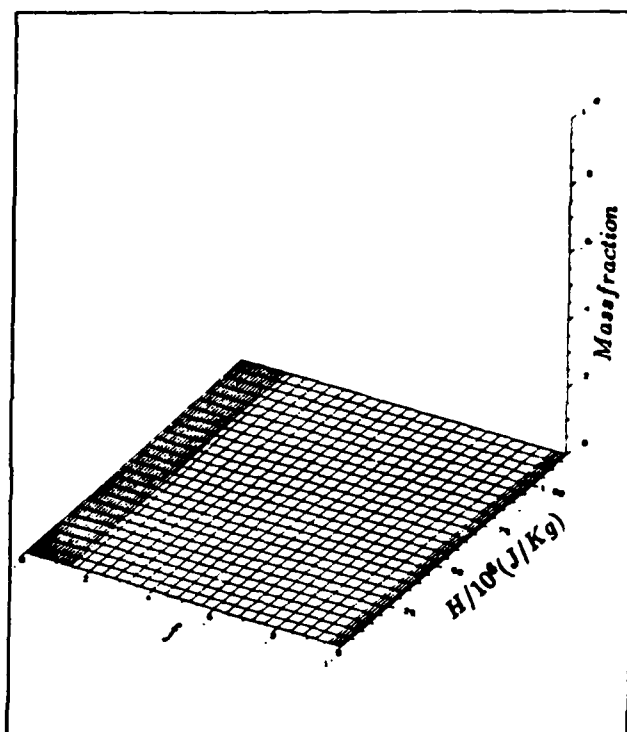
Figure 18: Y(NA,S) distribution with different f and H
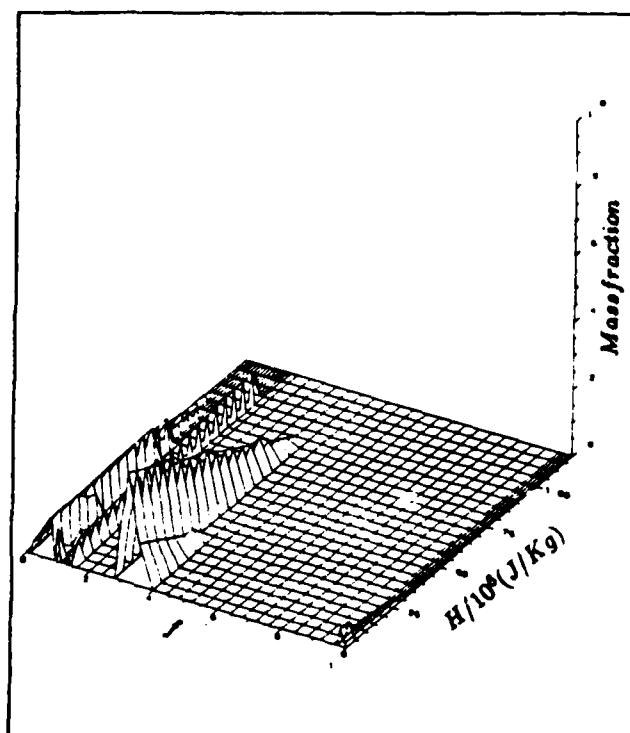
Figure 19: Y(NACL,S) distribution with different f and H
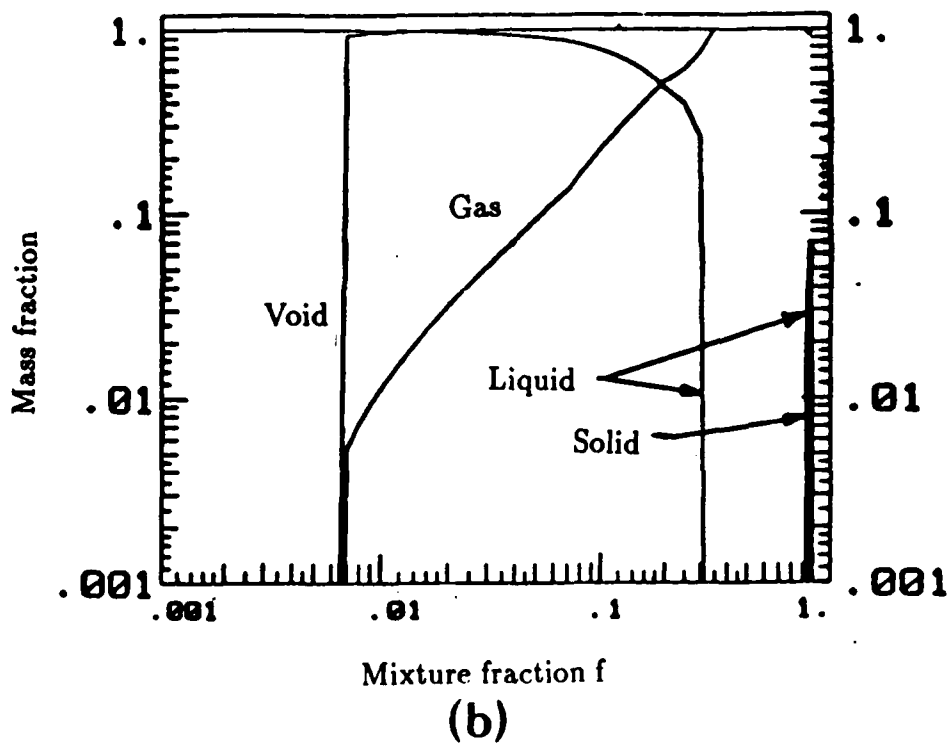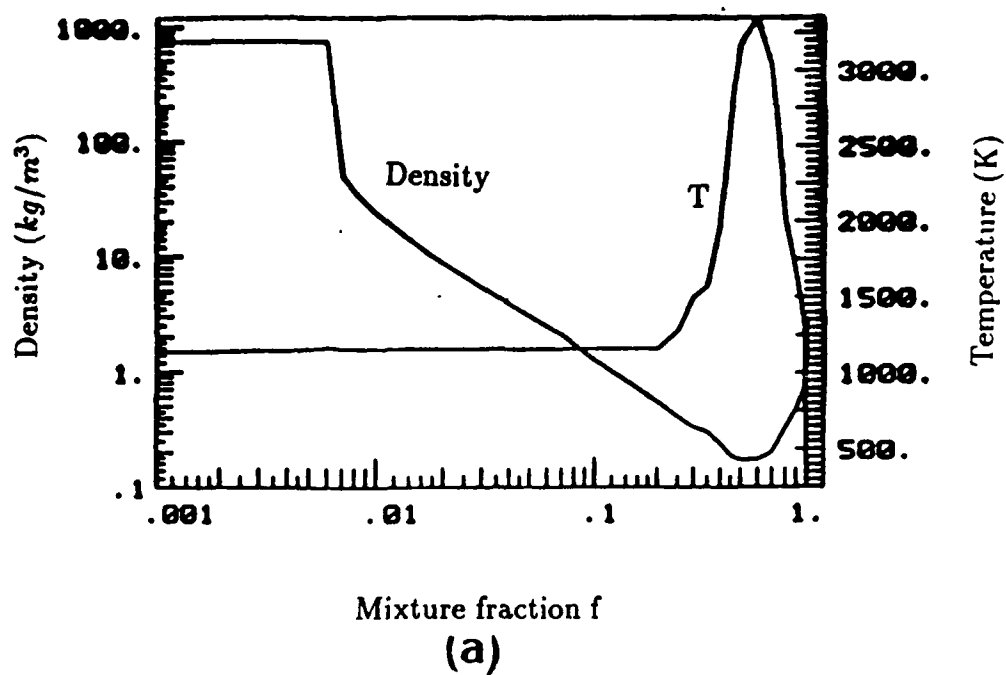
Figure 20:Temperature, density and mass fraction distribution with mixture fraction
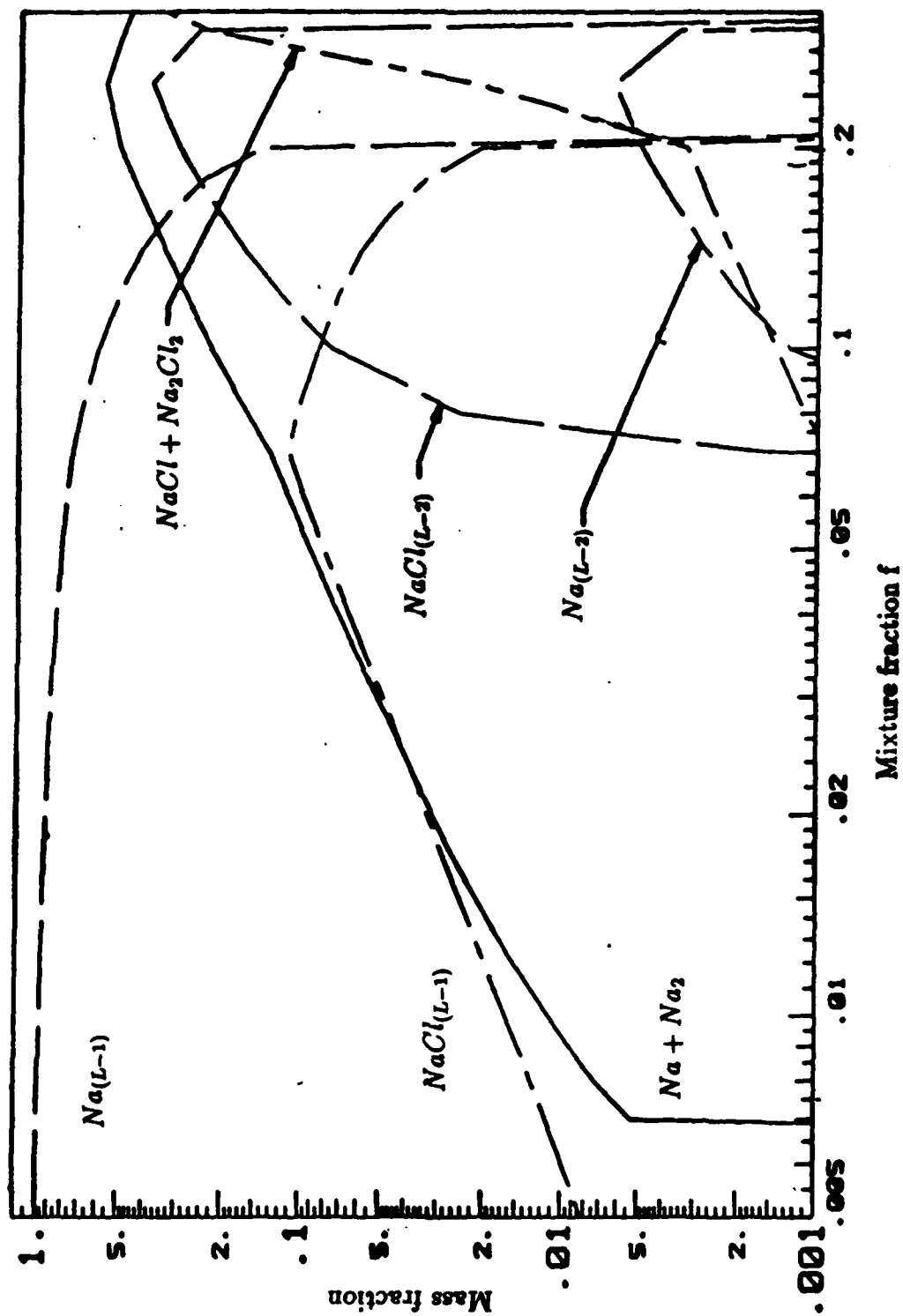
Figure 21:Mass fraction distribution with mixture fraction
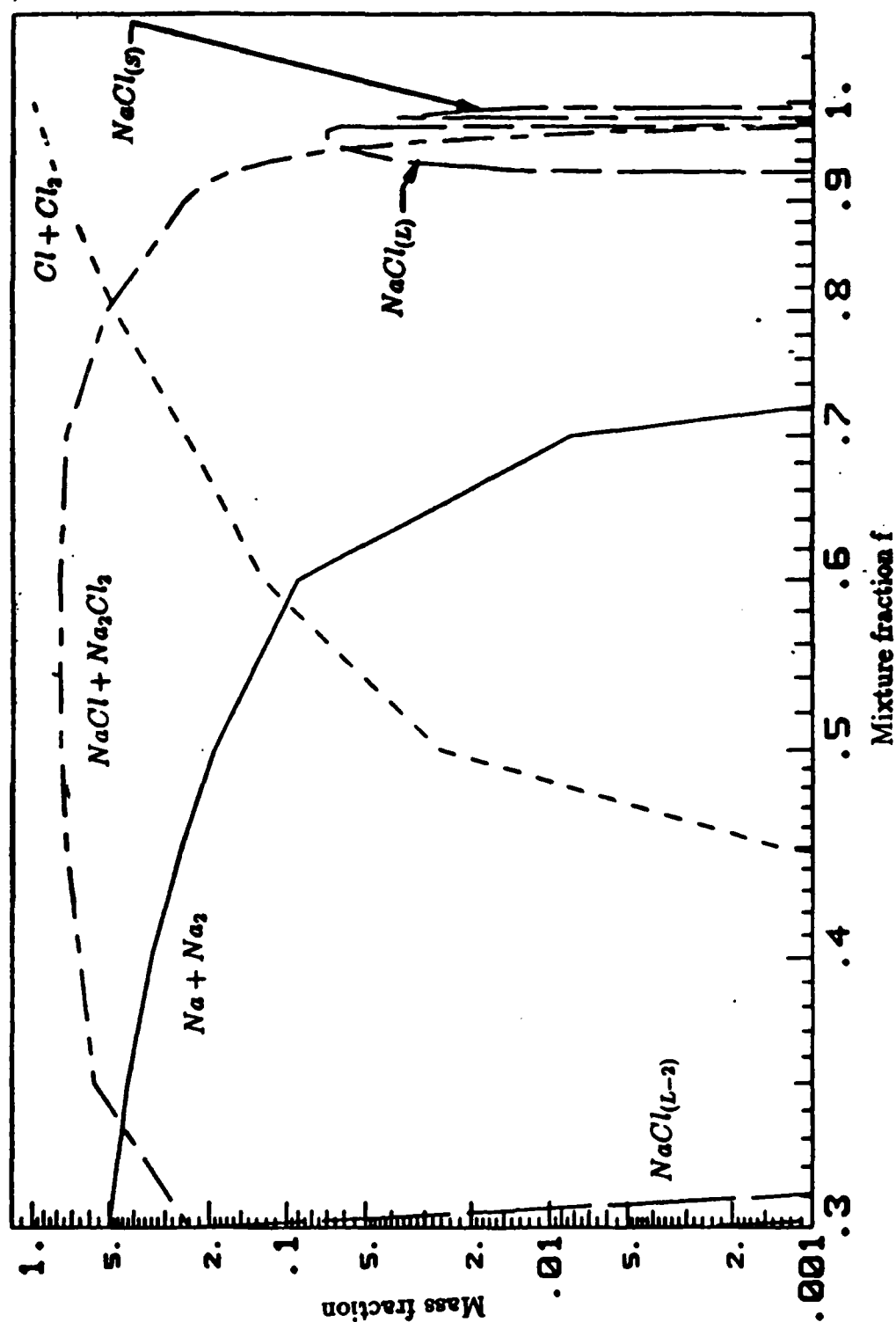
Figure 22 Mass fraction distribution with mixture fraction
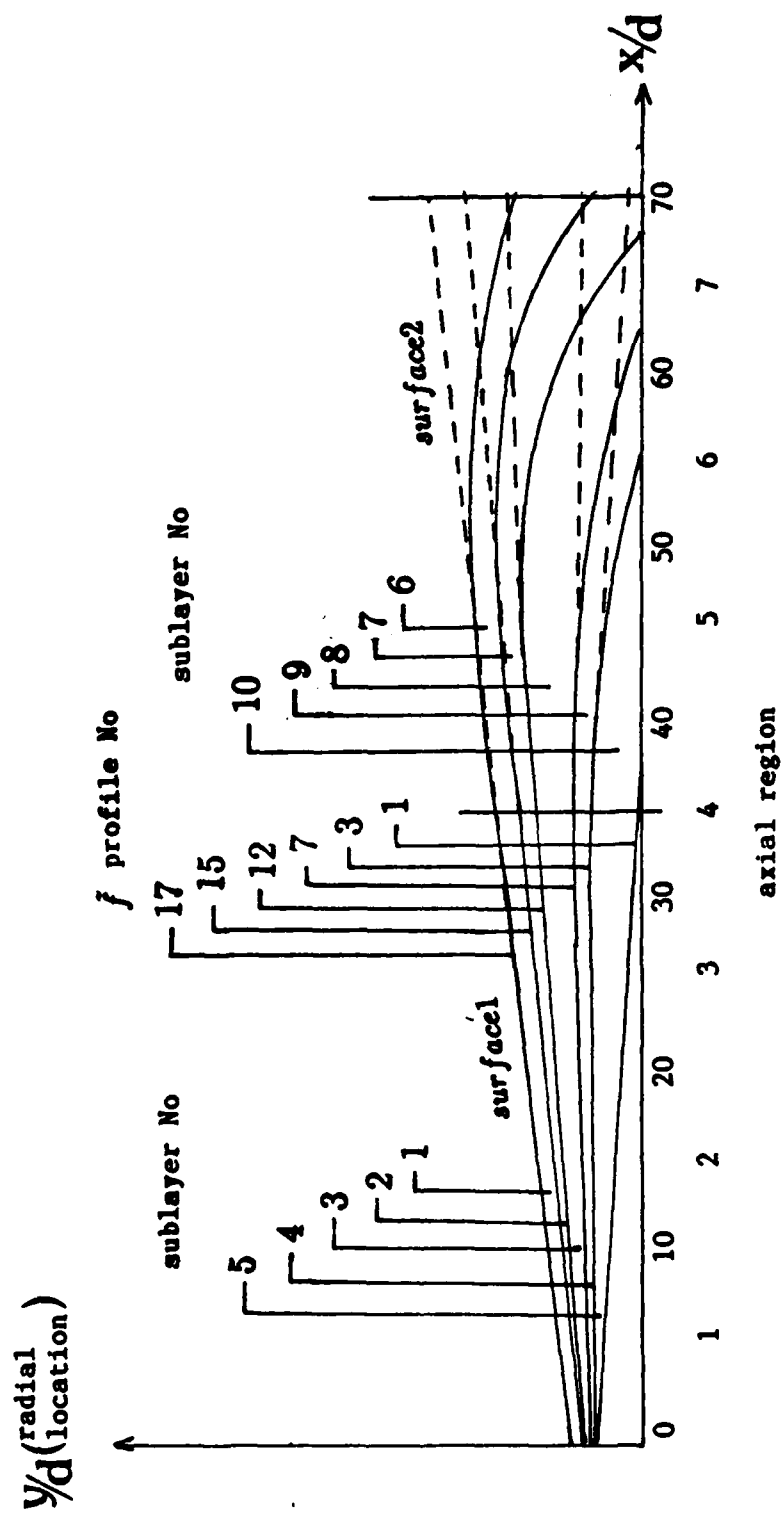
Figure 23: Averaged temperature sublayer in the combusting field

————— : actual flame profile

— — — : assumed flame profile

Figure 24: Variations of mean properties of temperature, mixture fraction, velocity, void fraction, gas phase, liquid phase and solid phase along the central axis

Figure 25: Variations of mean properties in gas phase along the central axis

$Na_{(L)} - Cl_{2,(G)}$ System, T_∞=1130K, T_0=298K, P_∞= 1 atm

Mean quantities along central axis

$\tilde{Y}_{NA,L-1}$

$\tilde{Y}_{NACL,L-1}$

$\tilde{Y}_{NACL,L-2}$

x/d
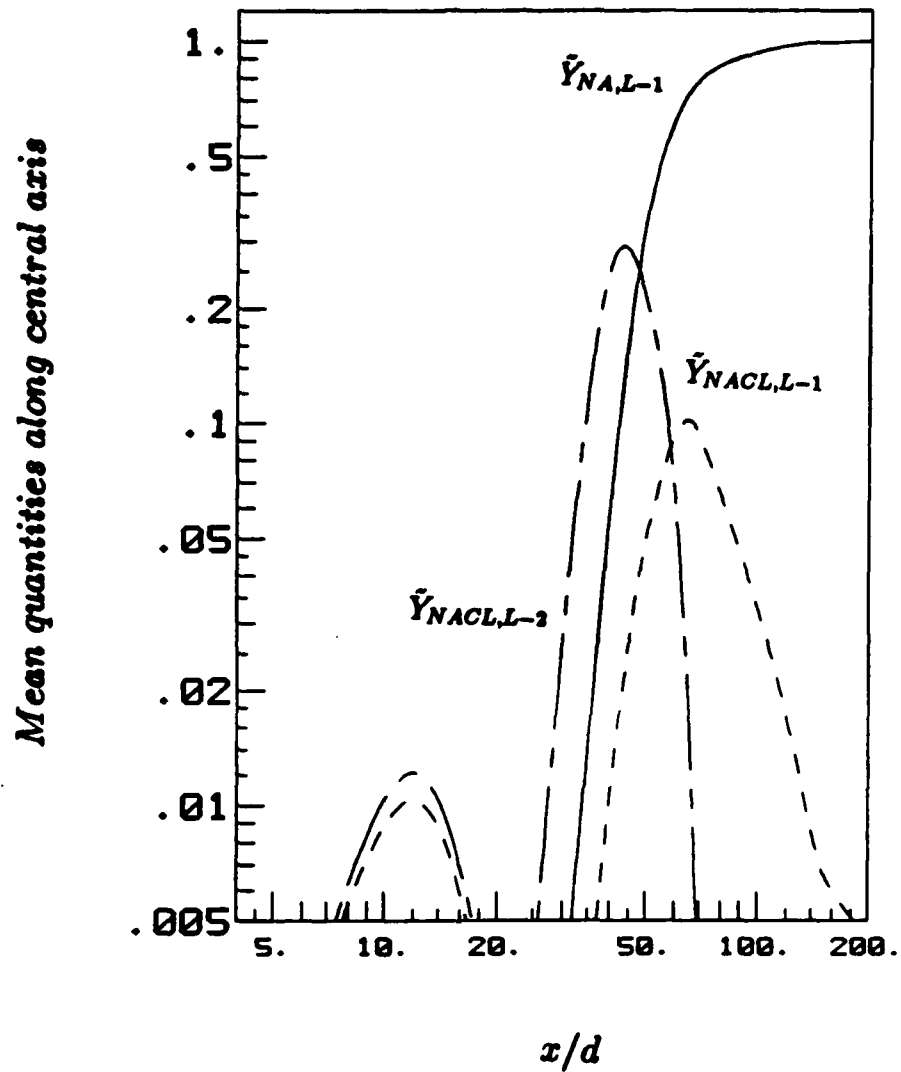
Figure 26: Variations of mean properties in liquid phase along the central axis
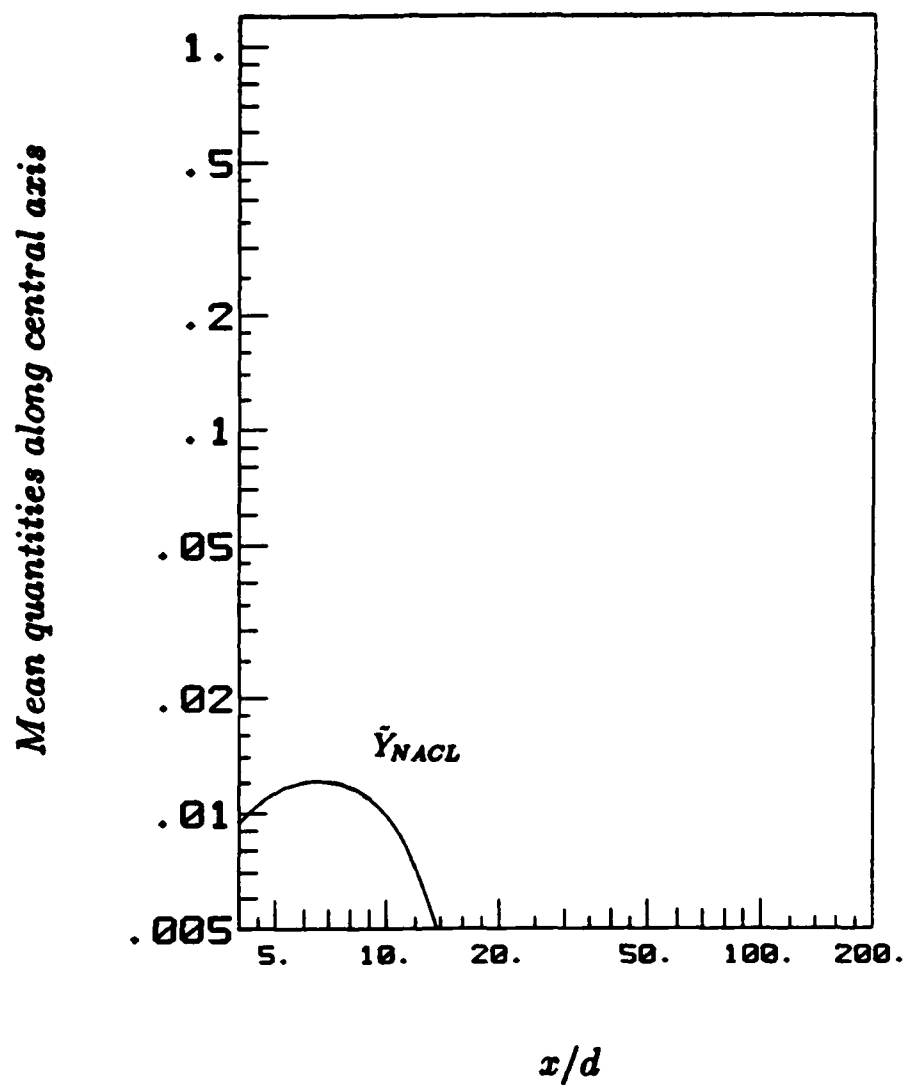
Figure 27:Variations of mean properties in solid phase along the central axis
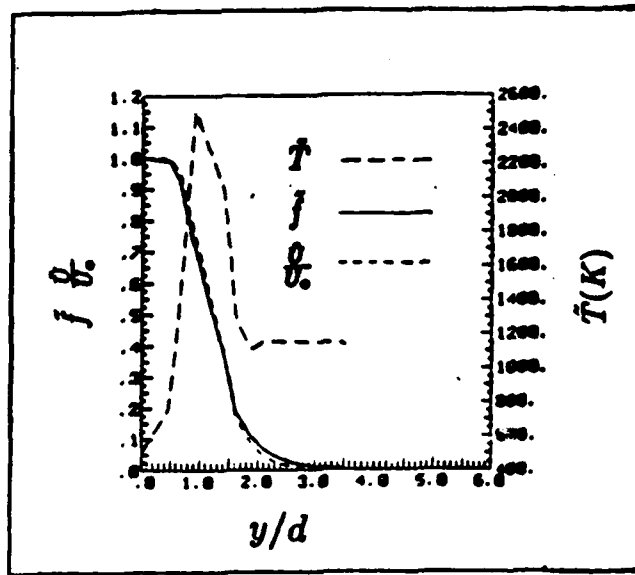
Figure 28: Variations of temperature, velocity and mixture fraction at $x/d=5$
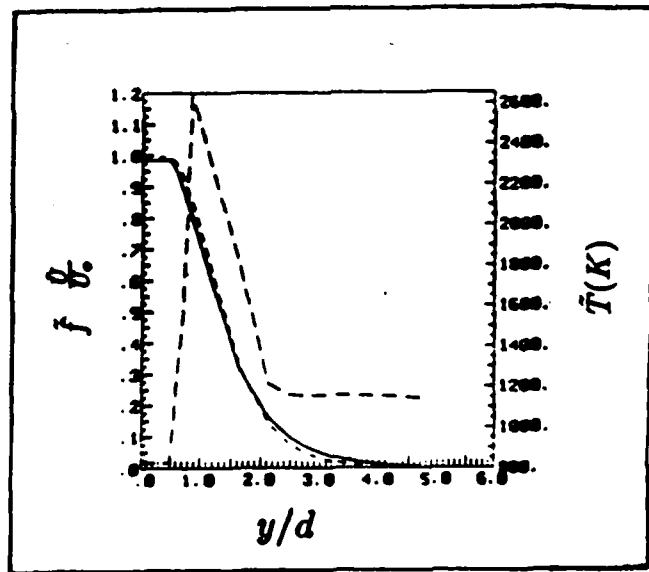
Figure 29: Variations of temperature, velocity and mixture fraction at $x/d=10$
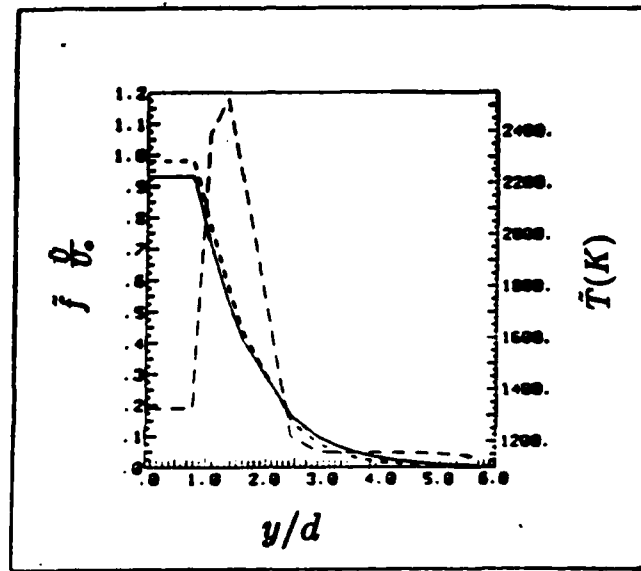
Figure 30: Variations of temperature, velocity and mixture fraction at x/d=15
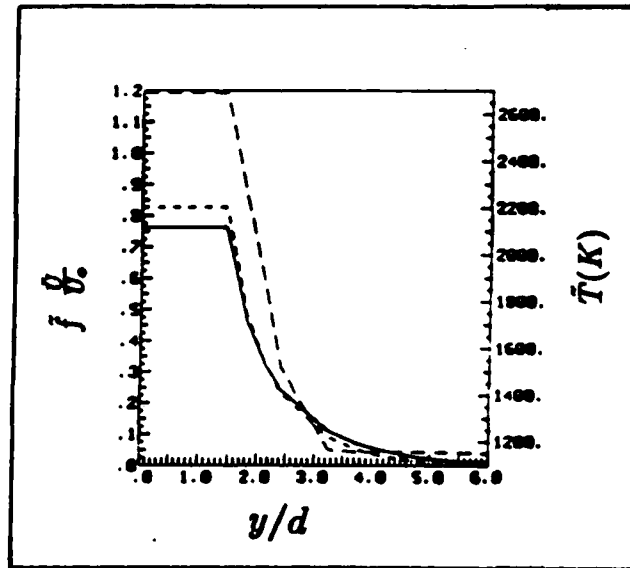
Figure 31: Variations of temperature, velocity and mixture fraction at x/d=20
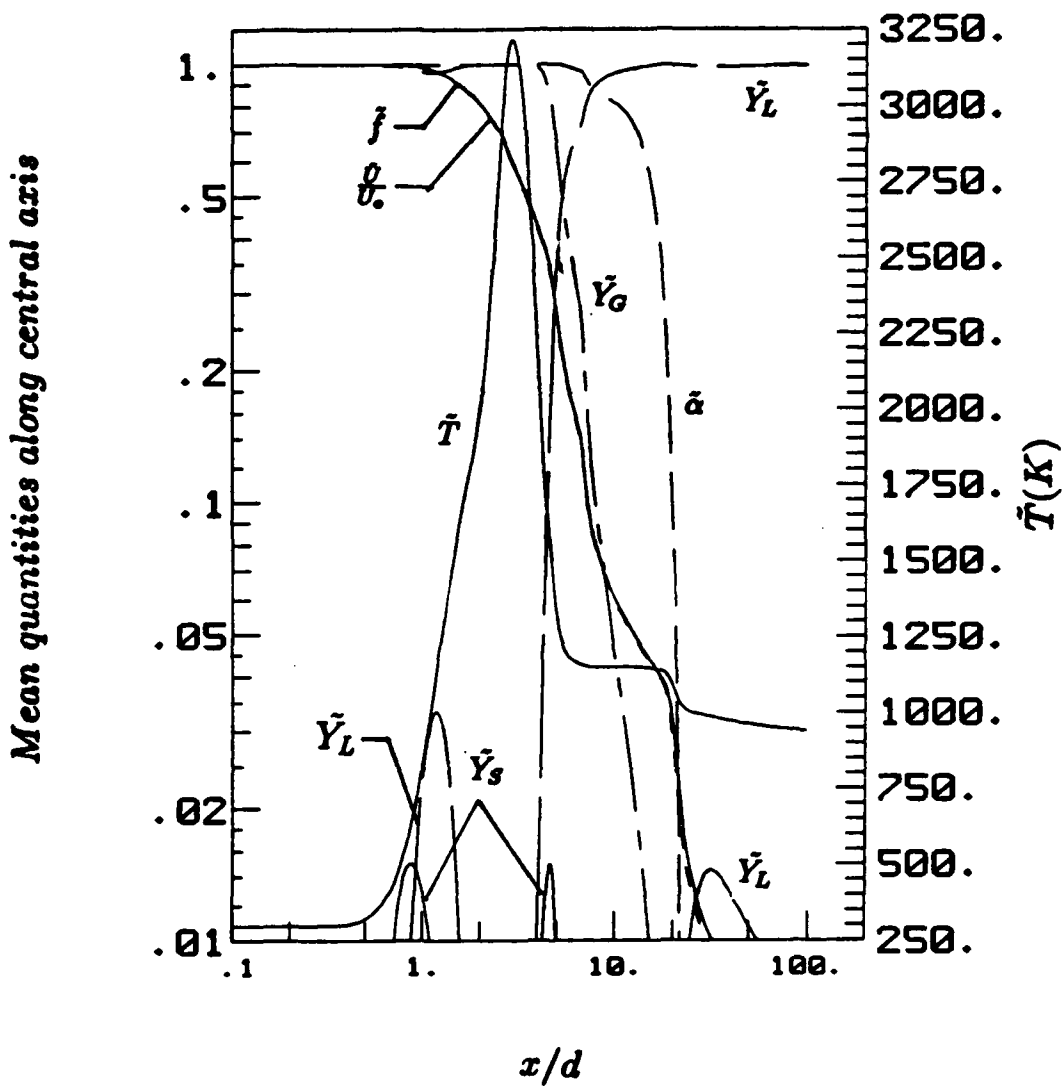
Figure 32: Variations of mean properties along the central axis due to subcooling effect
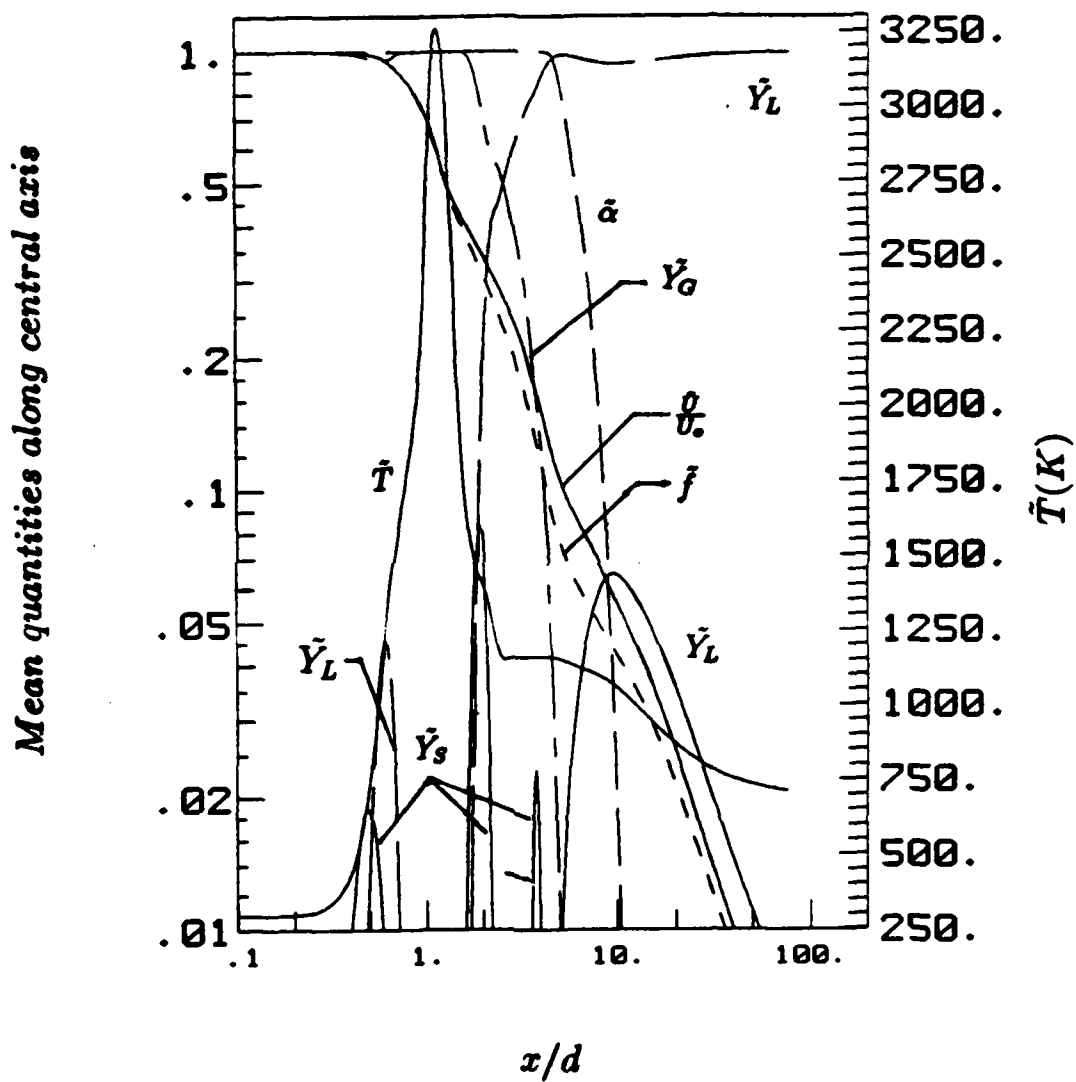
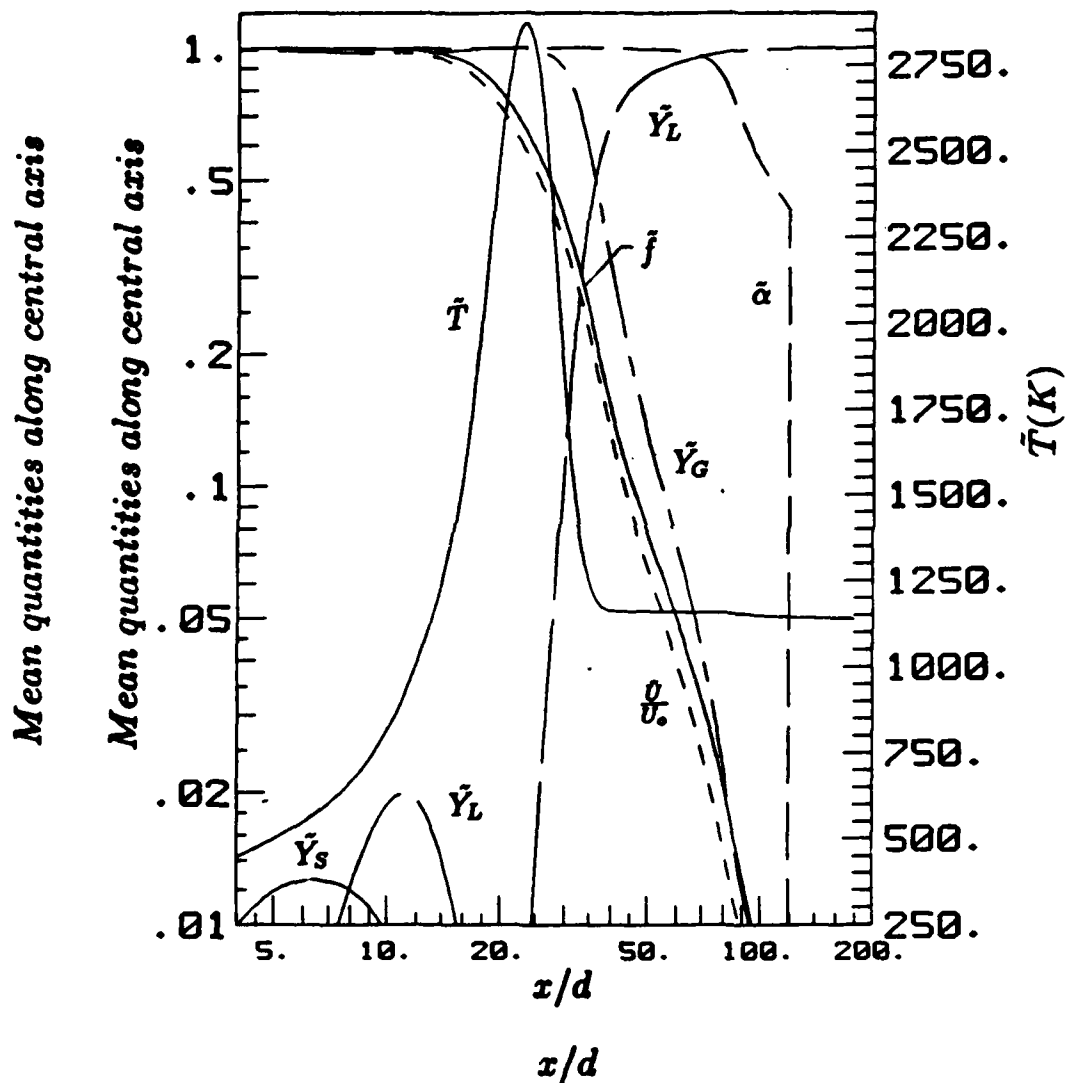Figure 33: Variations of mean properties along the central axis due to subcooling effect

Figure 34: Variations of mean properties of temperature, mixture fraction, velocity, void fraction, gas phase, liquid phase and solid phase along the central axis with radiation

Figure 35: Variations of mean properties in gas phase along the central axis with radiation

Figure 36: Variations of mean properties in liquid phase along the centralaxis with radiation
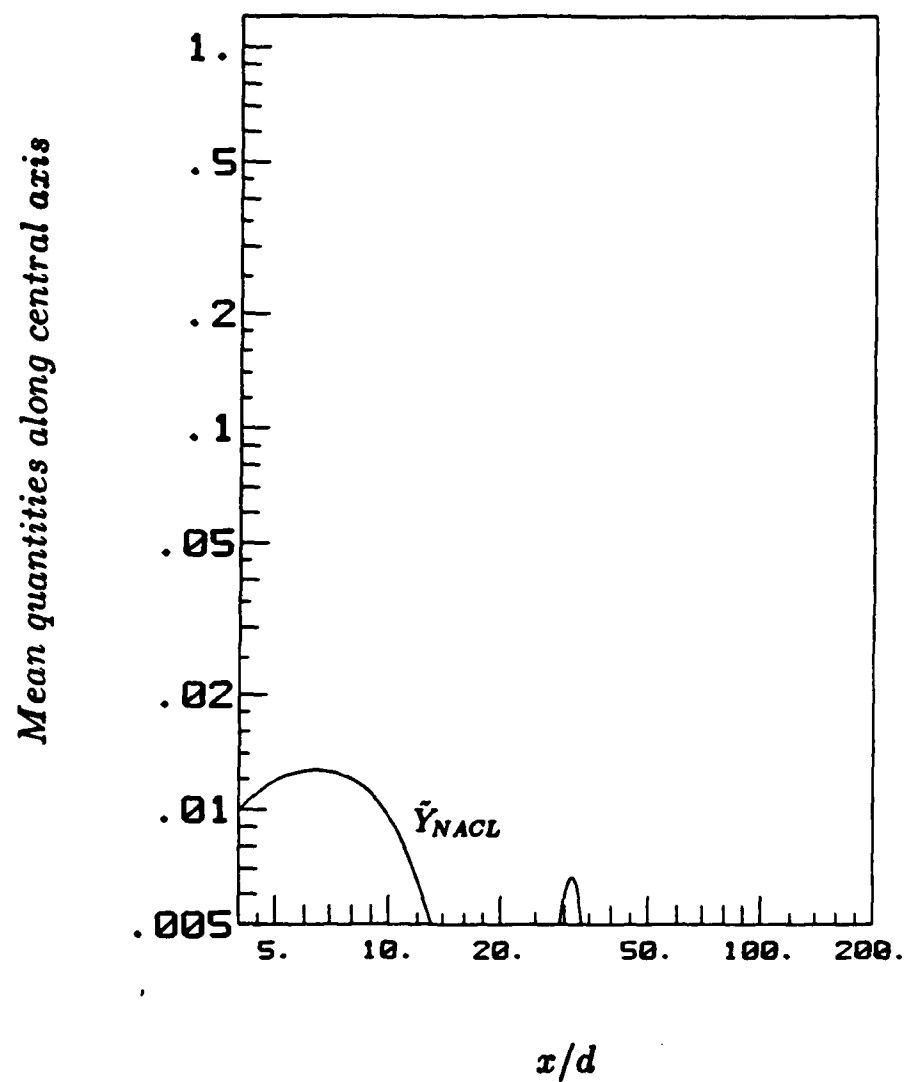
Figure 37: Variations of mean properties in solid phase along the central axis with radiation
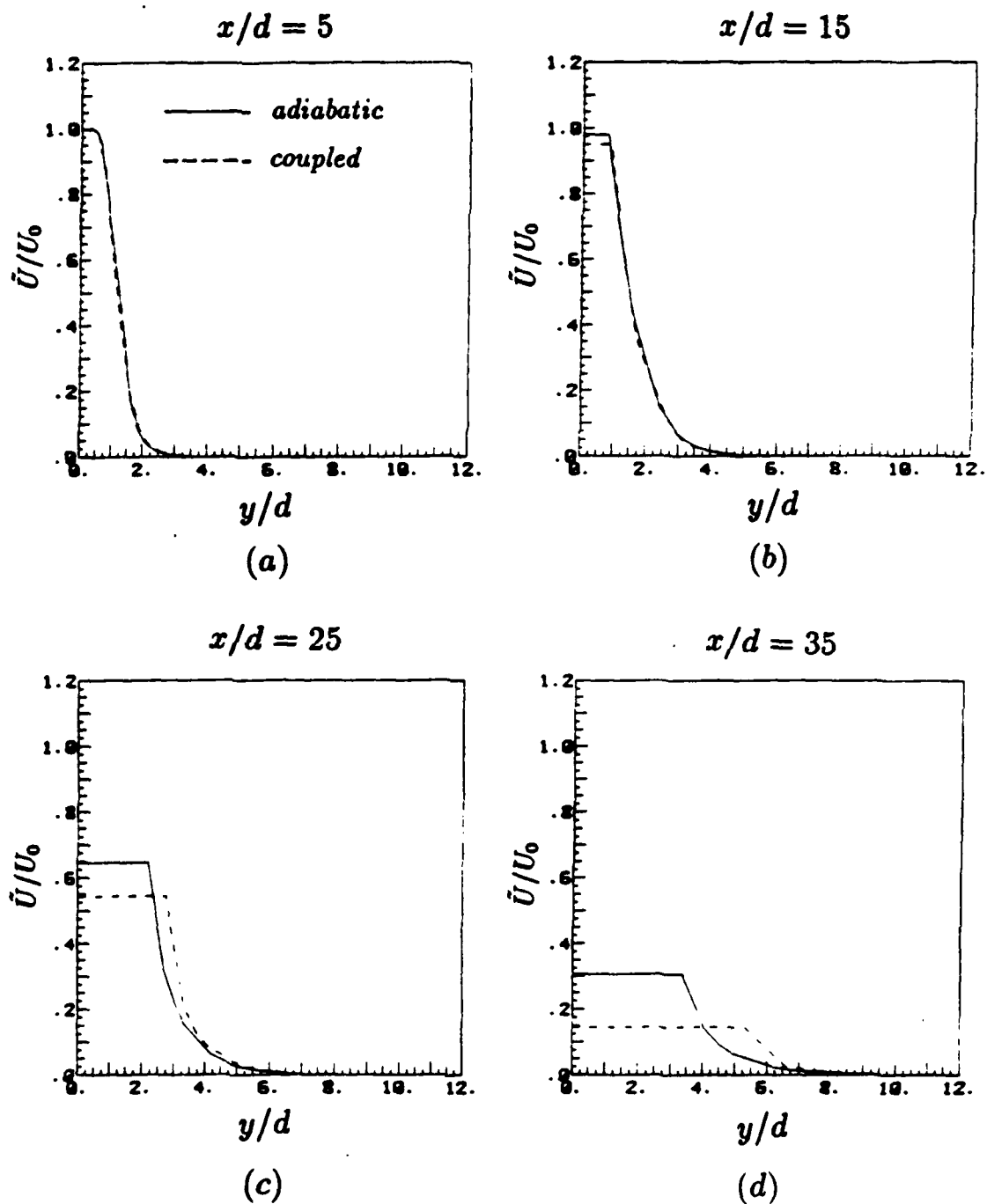
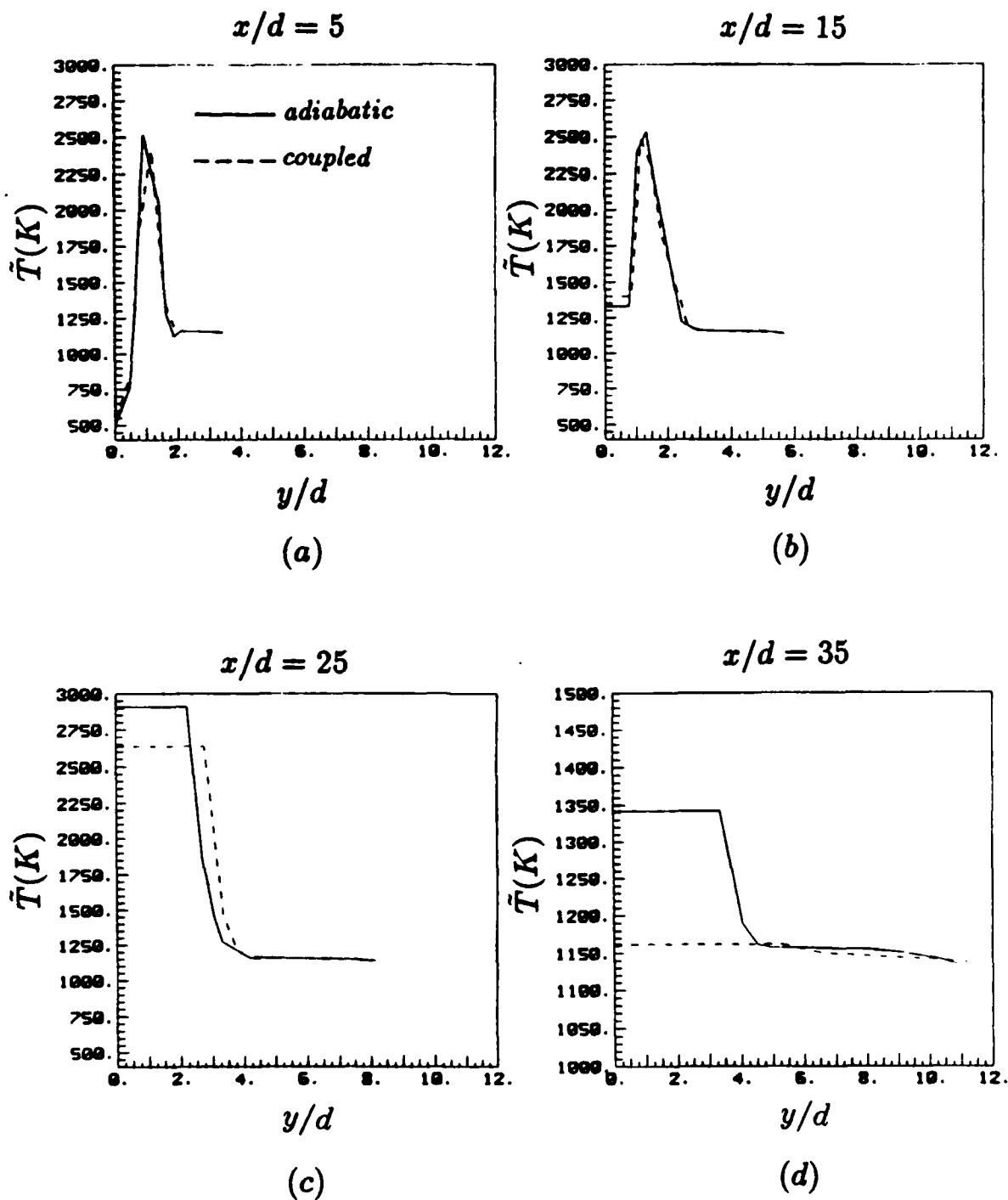Figure 38: Comparison of velocity along radial direction at different x/d between coupled and adiabatic analyses

Figure 39: Comparison of temperature along radial direction at different x/d between coupled and adiabatic analyses
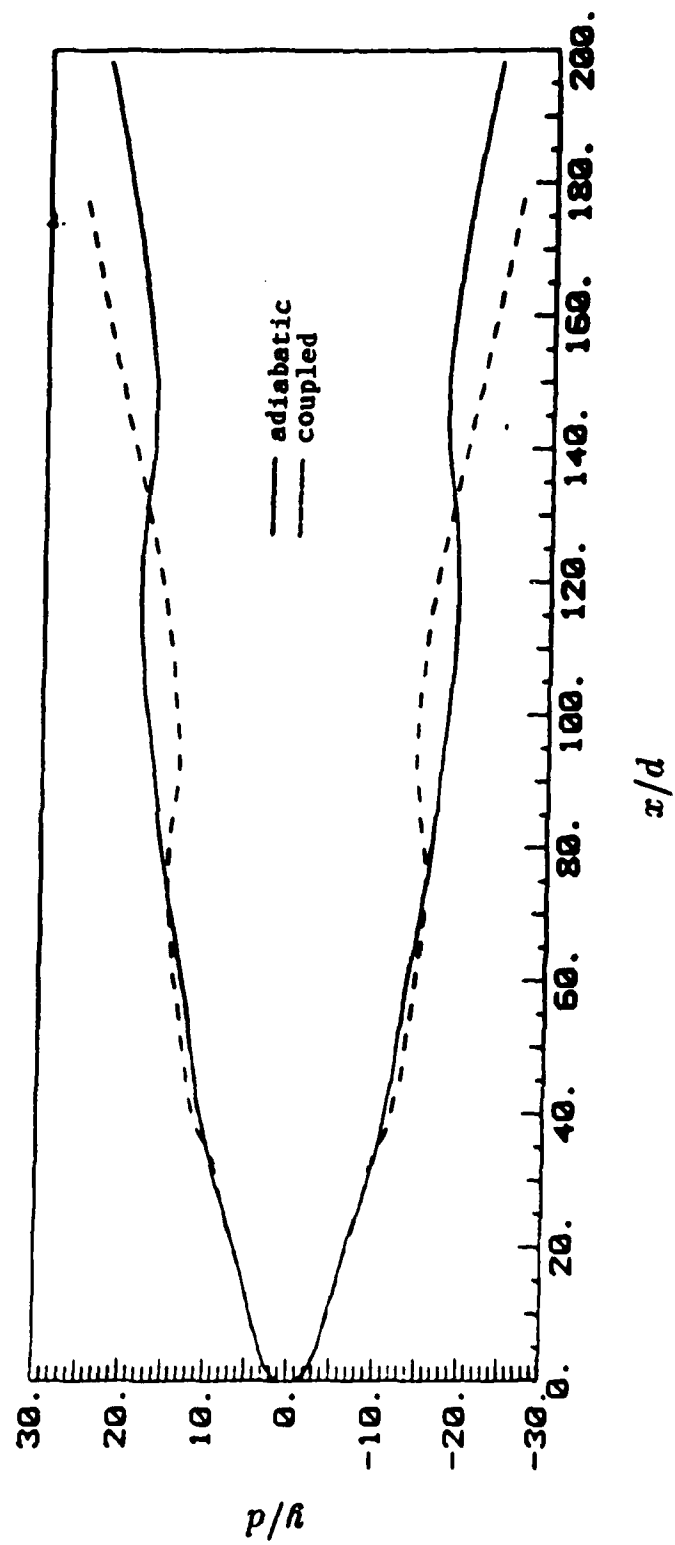
Jet Profile

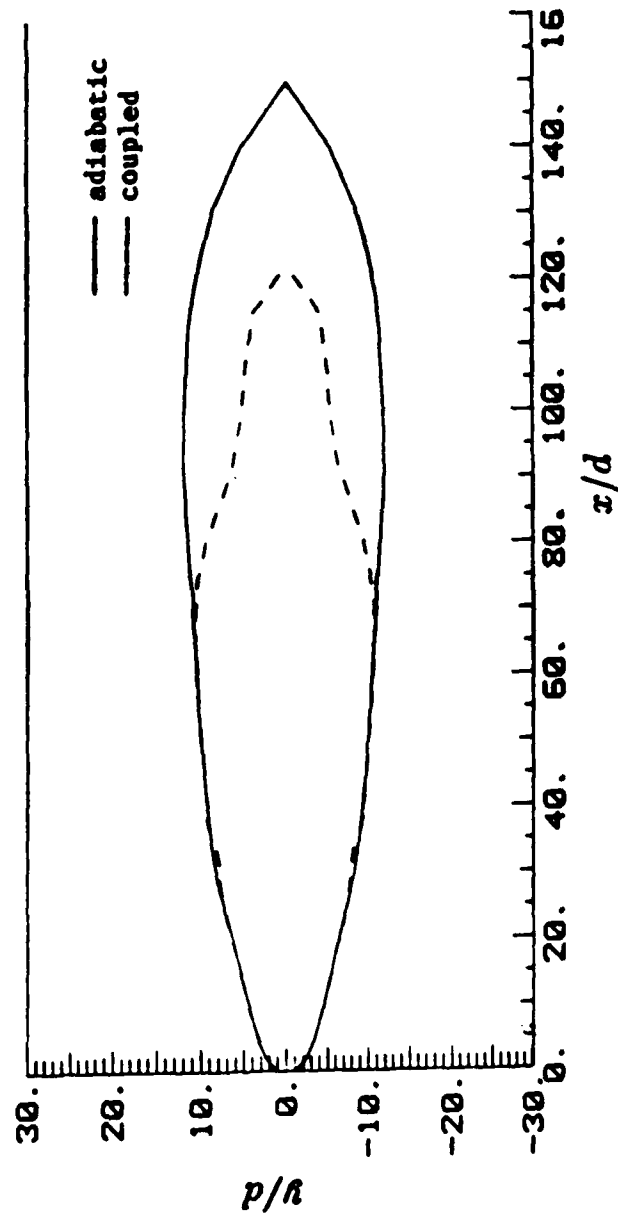Figure 40: Comparison of jet profile between coupled and radiation analyses

Figure 41: Comparison of plume length between adiabatic and coupled analyses

ONR REPORT DISTRIBUTION LIST CLOSED,
LIQUID METAL COMBUSTION*

Dr. Gabriel D. Roy (2)
Mechanics Division, Code 1132 P
Office of Naval Research
800 N. Quincy Street
Arlington, VA 22217-5000

Dr. Richard S. Miller (2)
Mechanics Division, Code 1132P
Office of Naval Research
800 N. Quincy Street
Arlington, VA 22217-5000

Dr. Lynn A. Parnell
Naval Ocean System Center
Code 6341
San Diego, CA 92152-5000

Defense Documentation Center (12)
Building 5, Cameron Station
Alexandria, VA 22314

Technical Information Division (6)
Naval Research Laboratory
4555 Overlook Avenue SW
Washington, DC 20375

Dr. Robert Nowark
Chemistry Division
Office of Naval Research
800 N. Quincy Street
Arlington, VA 22217

Dr. Albert D. Wood
Technology Programs
Office of Naval Research
800 N. Quincy Street
Arlington, VA 22217

Dr. H. W. Carhart
Combustion and Fuels
Naval Research Laboratory
Washington, DC 20375

Professor Allen Fuhs
Department of Aeronautics
Naval Post Graduate School
Monterey, CA 93943

Division Director
Engineering and Weapons
US Naval Academy
Annapolis, MD 21402

Mr. Francis J. Ramano
Code 63R3
Naval Sea Systems Command
Washington, DC 20363

Dr. Jerry A. Smith
Chemistry Division
Office of Naval Research
800 N. Quincy Street
Arlington, VA 22217

Mr. Robert Tampkins
Code 36621, Bldg. 1261
Naval Underwater System Center
Newport, RI 02841

Mr. Maurice F. Murphy
Code R33, Room 4-1711
Naval Surface Weapons, White Oak
Silver Spring, MD 20910

Dr. Kurt Mueller
Code R10
Energetic Materials Division
Naval Surface Weapons Center,
White Oak
Silver Spring, MD 20910

Dr. Earl Quandt, Jr.
Code 2704
David Taylor Naval Ship
Research and Development Center
Annapolis, MD 21402

---

*One copy except as noted in parenthesis.

Mr. Richard Bloomquist
Code 2752
David Taylor Naval Ship
Research and Development Center
Annapolis, MD 21402

Dr. Lawrence P. Cook
High Temperature Processes Group
National Bureau of Standards
Washington, DC 20234

Professor A. Murty Kanury
Department of Mechanical Engineering
Oregon State University
Corvallis, OR 97331

Professor Irvin Glassman
Department of Mechanical and
Aerospace Engineering
Engineering Quadrangle
Princeton University
Princeton, NY 08544

Dr. W. Lee
Research and Technology Department
Naval Surface Weapons Center
Silver Springs, MD 20703

Professor Norman Chigier
Department of Mechanical Engineering
Carnegie-Mellon University
Pittsburgh, PA 15213

Professor George Janz
Cogswell Laboratory, R306
Department of Chemistry
Rensselaer Polytechnic Institute
Troy, NY 12181

Dr. Leonard Leibowitz
Chemical Technology Division
Argonne National Laboratory
9700 South Cass Avenue
Argonne, IL 60439

Professor John Tarbell
104 Fenske Laboratory
Pennsylvania State University
University Park, PA 16801

Professor Thomas E. Daubert
104 Fenske Laboratory
Pennsylvania State University
University Park, PA 16801

Dr. J. Braunstein
Research Division
Oak Ridge Operations
Department E
Oak Ridge, TN 37831

Dr. Hugh H. Darsie
Advanced Technology Group
Sundstrand Energy Systems
4747 Harrison Avenue
Rockford, IL 61101

Professor Gerard M. Faeth
Department of Aerospace
Engineering
University of Michigan
Ann Arbor, MI 48109

Mr. Ron Kassing
MSI 207-4P
Fluid System Division
Allied Signal Corp.
1300 West Warner Rd.
P.O. Box 22200
Tempe, AZ 85285

Dr. Daniel H. Kiely
Power and Energy Group
Pennsylvania State University
Applied Research Laboratory
P.O. Box 30
State College, PA 16801

Professor Darryl E. Metzger
Department of Mechanical
and Aerospace Engineering
Arizona State University
Tempe, AZ 85281

Professor George A. Brown
Department of Mechanical Engineering
and Applied Mechanics
University of Rhode Island
Kingston, RI 02881

Professor Paul E. Dimontakis
Mail Code 301-46
Graduate Aeronautical Laboratory
California Institute of Technology
Pasadena, CA 91125

Dr. Charles H. Berman
Aerochem Research Laboratories, Inc.
P.O. Box 12
Princeton, NJ 08542

Dr. Donald M. McEligot
Westinghous Naval System Division
62 Johnny Cake Hill
Middletown, RI 02840

Dr. C. William Kauffman
Department of Aerospace Engineering
The University of Michigan
Ann Arbor, MI 48109-2140

Professor Lea D. Chen
Department of Mechanical Engineering
The University of Iowa
Iowa City, IA 5542

LCDR Mike Barry
NISC - 4311
Naval Intelligence Support Center
4301 Suitland Road
Washington, DC 20390

Dr. Raafat H. Guirguis
Laboratory for Computational
Physics
Code 4040
Naval Research Laboratory
Washington, DC 20375

Professor John Cimbala
157 Hammond Bldg.
Department of Mechanical Engrg.
Pennysylvania State University
University Park, PA 16802

Mr. David White
Manager of Advanced Development
Solar Turbine Inc.
2200 Pacific Highway
P.O. Box 85376
San Diego, CA 92138-5376

Mr. William J. Greenlee
Engineering Manager Research
Department 741A6, Sundstrand ATG
4747 Harrison Avenue
P.O. Box 7002
Rockford, IL 61125-7002